Dynamo action in the ABC flows using symmetries

Samuel E. Jones & Andrew D. Gilbert

Mathematics Research Institute,
College of Engineering, Mathematics and Physical Sciences,
University of Exeter, EX4 4QF, U.K.

Abstract

This paper concerns kinematic dynamo action by the 1:1:1 ABC flow, in the highly conducting limit of large magnetic Reynolds number R_m. The flow possesses 24 symmetries, with a symmetry group isomorphic to the group O_{24} of orientation-preserving transformations of a cube. This can be exploited to break up the linear eigenvalue problem into five distinct symmetry classes, or irreducible representations, which we label I–V. The paper discusses how to reduce the scale of the numerical problem to a subset of Fourier modes for a magnetic field in each representation, which then may be solved independently to obtain distinct branches of eigenvalues and magnetic field eigenfunctions.

Two numerical methods are employed: the first is to time step a magnetic field in a given symmetry class and obtain the growth rate and frequency by measuring the magnetic energy as a function of time. The second method involves a more direct determination of the eigenvalue using the eigenvalue solver ARPACK for sparse matrix systems, which employs an implicitly restarted Arnoldi method. The two methods are checked against each other, and compared for efficiency and reliability. Eigenvalue branches for each symmetry class are obtained for magnetic Reynolds numbers R_m up to 10^4 together with spectra and magnetic field visualisations. A sequence of branches emerges as R_m increases and the magnetic field structures in the different branches are discussed and compared. In a parallel development, results are presented for the corresponding fluid stability problem as a function of the Reynolds number R_e.

Key words: kinematic dynamo, ABC flow, fast dynamo, Arnoldi method

21 March 2014

1 Introduction

The ABC flows are well-known three-dimensional flows defined by

$$\boldsymbol{u} = (C\sin z + B\cos y, A\sin x + C\cos z, B\sin y + A\cos x) \tag{1.1}$$

with $A, B, C \in \mathbb{R}$, and x, y and z periodic, period 2π. They are steady, incompressible solutions to the Euler equation whose flow properties depend on the choice of the three parameters, as discussed in Dombre *et al.* (1986), where the term 'ABC flows' was coined. These flows are discussed in Arnold (1965), as a case of three-dimensional Euler flows that have a simple description in the Eulerian framework, but that could have chaotic trajectories in the Lagrangian sense. Hénon (1966) went on to provide numerical evidence of chaos in members of the family, with further work by Dombre *et al.* (1986) who consider integrability of streamlines using Painlevé tests. This Lagrangian complexity and the fact that these are Beltrami flows, for which $\nabla \times \boldsymbol{u} = k\boldsymbol{u}$, makes them of great interest in both hydrodynamics and magnetohydrodynamics. Our aim is to obtain numerical results for linear dynamo action and fluid stability for the case $A = B = C = 1$, that is the 1:1:1 ABC flow, by exploiting its large collection of symmetries.

Although Childress (1970) used the 1:1:1 ABC flow as a prototype dynamo giving growth of magnetic fields on large scales through an isotropic alpha effect, the first numerical investigation of kinematic dynamo action in this flow was undertaken by Arnold & Korkina (1983), who consider magnetic fields with the same 2π periodicity as the flow. Their results show that a range of values of R_m exists for which such magnetic fields grow, defining the first 'window' of dynamo action for the 1:1:1 flow. Galloway & Frisch (1986) extended these results to $R_m = 550$ and discovered a second window of dynamo activity, showing that the magnetic field in this second window has lost many of the symmetries that exist in the first. This and more recent work (Lau & Finn, 1992; Galloway & O'Brian, 1994; Archontis & Dorch, 1999; Archontis *et al.*, 2003) focuses on the geometry of the resulting fields and finds that they are dominated by cigars, regions of concentrated magnetic field, though the different windows correspond to different configurations of these structures. Additionally, it appears that the growth rate of the 1:1:1 dynamo approaches a limiting value in the range of R_m up to 550, suggesting that it is a fast dynamo, with a growth rate bounded above zero in the high conductivity limit $R_m \to \infty$. Very recently, however, Bouya & Dormy (2013) have shed more light on the 1:1:1 ABC dynamo, with simulations up to $R_m = 2.5 \times 10^4$, and show that the growth rate continues to change when R_m is increased further, as we shall discuss below. For a recent perspective on ABC dynamos, see Galloway (2012).

The ABC flows possess discrete helical symmetries (rotation combined with translation), inherited from the continuous helical symmetry of the individual helical waves in (1.1). The number of symmetries depends on the parameters A, B and C (see Dombre *et al.*, 1986). Maximal symmetry occurs for equal parameters, that is in the 1:1:1 case, for which there are a total of 24 orientation-preserving symmetries. These are set out in Arnold (1984), which also describes how a field, for example written as a sum of Fourier modes, may be decomposed into distinct symmetry classes. Each symmetry class is known technically as an irreducible representation and there are five of these, which we label I–V. Thus the evolution of any magnetic field under the 1:1:1 ABC flow can be broken up into a sum of copies of five distinct types of fields. Arnold (1984) reproduced the results of Arnold & Korkina (1983) for $R_m < 5$, using a severely truncated (5 mode) model for fields in representation II, which is the relevant symmetry class

for the first window of dynamo action. Gilbert (1992) considered a simplified ABCS dynamo ($A = B = 1$, $C \ll 1$), and how a magnetic field that belongs to a single representation can be constructed from a general field using the symmetries of the flow (see the D_8 example in §2 for more information). The results for this flow show a growth rate dependent on the initial field used, as fields in representations that are odd under the reflection operation s in D_8 are amplified, unlike fields that are even under s; these fields are visualised in Matthews (1999).

As well as the interest in the complex Lagrangian properties of the ABC flows for dynamo action, a parallel research direction concerns the linear hydrodynamic stability of these flows, when considered as steady, forced solutions to the Navier–Stokes equation at a given Reynolds number R_e. By introducing a velocity perturbation to an ABC flow in the Navier-Stokes equation, a linear equation analogous to the kinematic dynamo problem is obtained, allowing hydrodynamic stability to be studied alongside the magnetic case with only minor modifications. Galloway & Frisch (1987) investigate the linear stability of several ABC flows, of which the 1:1:1 flow appears to be the most stable, initially becoming unstable at $R_e \approx 14$ with the growth rate appearing to reach an asymptote by $R_e = 200$. The resulting perturbations may also be classified through their symmetries, in the same way as for the magnetic problem.

For this hydrodynamic problem with an ABC 1:1:1 forcing, Podvigina (1999) breaks up the resulting dynamical system into sub-systems with different symmetries. In a similar manner to Arnold (1984), she discusses how Fourier modes are partitioned into the various representations in the linear regime. Further exploration of the nonlinear dynamics is given in Ashwin & Podvigina (2003), where the symmetries of bifurcations and branches of solutions are identified by comparing mode values with those expected for each symmetry class. It is important to note that in these nonlinear problems symmetry breaking mechanisms can link branches of fields with different symmetries (for example, see Podvigina & Pouquet, 1994). In fact in the full nonlinear regime several aspects of the analysis are different from the linear problem, since linear combinations of fields may no longer be freely taken. However in the kinematic 1:1:1 ABC dynamo which we study here, the problem is linear and the magnetic fields of the five representations are entirely independent. This allows each of the five types of field to be studied separately: we can fully impose the symmetries, restricting the fields to a single representation. The evolution of a general field will just be a linear combination of these.

We outline the structure of the paper and the topics addressed. We first discuss in §2 the governing equations for the 1:1:1 ABC dynamo problem and the equivalent fluid stability problem. In §3 we illustrate representation theory in the case of the group D_8 (symmetries of a square) and explain how a field can be decomposed into five distinct irreducible representations or symmetry classes (in what follows we use the terms interchangeably). We then give the corresponding results for the symmetry group O_{24} of the 1:1:1 ABC flow. The reader with knowledge of representation theory may wish to omit this section. In §4 numerical methods for the dynamo problem are given, and it is explained how the use of representation theory can reduce the size of the numerical problem by only time stepping a subset of Fourier modes. In the latter half of this section, an alternative approach to time stepping, namely employing an eigenvalue solver using an Arnoldi iteration algorithm, is considered and a comparison is drawn between the two methods. In section §5 we give results for the ABC dynamo, with a comparison of the growth rates and frequencies of fields in each representation. The features and structures of the dominant field in each representation are visualised. In the following section §6, the corresponding results for the linear fluid stability problem are set out. Our final section §7 gives concluding discussion and comments.

2 Governing equations and symmetries

We are interested in kinematic dynamo action in the 1:1:1 ABC flow given by

$$\boldsymbol{u} = (\sin z + \cos y, \sin x + \cos z, \sin y + \cos x). \tag{2.1}$$

This has the Beltrami property that $\boldsymbol{u}$ and $\nabla \times \boldsymbol{u}$ are everywhere parallel, and in fact the two fields are equal, with $0 = \boldsymbol{u} \times (\nabla \times \boldsymbol{u}) = \frac{1}{2}\nabla|\boldsymbol{u}|^2 - \boldsymbol{u} \cdot \nabla \boldsymbol{u}$. A magnetic field evolves according to the induction equation given by

$$\partial_t \boldsymbol{b} + \boldsymbol{u} \cdot \nabla \boldsymbol{b} = \boldsymbol{b} \cdot \nabla \boldsymbol{u} + \varepsilon \nabla^2 \boldsymbol{b}, \tag{2.2}$$

where $\varepsilon \equiv R_m^{-1}$ is the dimensionless diffusivity or inverse magnetic Reynolds number, and $\nabla \cdot \boldsymbol{b} = \nabla \cdot \boldsymbol{u} = 0$.

We are also concerned with the corresponding fluid stability problem, in which the steady ABC flow $\boldsymbol{u}$ above is taken to be maintained against viscosity by a body force $\boldsymbol{f} = -\varepsilon \nabla^2 \boldsymbol{u} = \varepsilon \boldsymbol{u}$. In the corresponding Navier–Stokes equation for a general flow $\boldsymbol{U}$,

$$\partial_t \boldsymbol{U} + \boldsymbol{U} \cdot \nabla \boldsymbol{U} = -\nabla P + \varepsilon \nabla^2 \boldsymbol{U} + \boldsymbol{f}, \tag{2.3}$$

we set $\boldsymbol{U} = \boldsymbol{u} + \boldsymbol{v}$ and $P = -\frac{1}{2}\boldsymbol{u}^2 + p$, where $\boldsymbol{v}$ is the perturbation velocity and p the perturbation pressure. In the linear approximation the field $\boldsymbol{v}$ obeys

$$\partial_t \boldsymbol{v} + \boldsymbol{u} \cdot \nabla \boldsymbol{v} + \boldsymbol{v} \cdot \nabla \boldsymbol{u} = -\nabla p + \varepsilon \nabla^2 \boldsymbol{v}, \tag{2.4}$$

with $\nabla \cdot \boldsymbol{v} = 0$. This has a very similar structure to the magnetic field problem, with $\varepsilon = R_e^{-1}$ as now an inverse Reynolds number.

We will always work within a 2π-periodic box for flows and magnetic fields. With this periodicity, the ABC flow field (2.1) is invariant under a group G with the following 24 symmetry transformations,

$$\begin{aligned}
\mathsf{i}(\boldsymbol{x}) &= (x, y, z), & \mathsf{a}(\boldsymbol{x}) &= (\tfrac{\pi}{2} - y, x + \tfrac{\pi}{2}, z - \tfrac{\pi}{2}), \\
\mathsf{a}^2(\boldsymbol{x}) &= (-x, \pi - y, z + \pi), & \mathsf{a}^3(\boldsymbol{x}) &= (y - \tfrac{\pi}{2}, \tfrac{\pi}{2} - x, z + \tfrac{\pi}{2}), \\
\mathsf{b}(\boldsymbol{x}) &= (x - \tfrac{\pi}{2}, \tfrac{\pi}{2} - z, y + \tfrac{\pi}{2}), & \mathsf{b}^2(\boldsymbol{x}) &= (x + \pi, -y, \pi - z), \\
\mathsf{b}^3(\boldsymbol{x}) &= (x + \tfrac{\pi}{2}, z - \tfrac{\pi}{2}, \tfrac{\pi}{2} - y), & \mathsf{c}(\boldsymbol{x}) &= (z + \tfrac{\pi}{2}, y - \tfrac{\pi}{2}, \tfrac{\pi}{2} - x), \\
\mathsf{c}^2(\boldsymbol{x}) &= (\pi - x, y + \pi, -z), & \mathsf{c}^3(\boldsymbol{x}) &= (\tfrac{\pi}{2} - z, y + \tfrac{\pi}{2}, x - \tfrac{\pi}{2}), \\
\mathsf{d}(\boldsymbol{x}) &= (z, x, y), & \mathsf{d}^2(\boldsymbol{x}) &= (y, z, x), \\
\mathsf{e}(\boldsymbol{x}) &= (-z, \pi - x, y + \pi), & \mathsf{e}^2(\boldsymbol{x}) &= (\pi - y, z + \pi, -x), \\
\mathsf{f}(\boldsymbol{x}) &= (z + \pi, -x, \pi - y), & \mathsf{f}^2(\boldsymbol{x}) &= (-y, \pi - z, x + \pi), \\
\mathsf{g}(\boldsymbol{x}) &= (\pi - z, x + \pi, -y), & \mathsf{g}^2(\boldsymbol{x}) &= (y + \pi, -z, \pi - x), \\
\mathsf{h}(\boldsymbol{x}) &= (\tfrac{\pi}{2} - x, z + \tfrac{\pi}{2}, y - \tfrac{\pi}{2}), & \mathsf{j}(\boldsymbol{x}) &= (z - \tfrac{\pi}{2}, \tfrac{\pi}{2} - y, x + \tfrac{\pi}{2}), \\
\mathsf{k}(\boldsymbol{x}) &= (y + \tfrac{\pi}{2}, x - \tfrac{\pi}{2}, \tfrac{\pi}{2} - z), & \mathsf{l}(\boldsymbol{x}) &= (-x - \tfrac{\pi}{2}, -z - \tfrac{\pi}{2}, -y - \tfrac{\pi}{2}), \\
\mathsf{m}(\boldsymbol{x}) &= (-z - \tfrac{\pi}{2}, -y - \tfrac{\pi}{2}, -x - \tfrac{\pi}{2}), & \mathsf{n}(\boldsymbol{x}) &= (-y - \tfrac{\pi}{2}, -x - \tfrac{\pi}{2}, -z - \tfrac{\pi}{2}).
\end{aligned} \tag{2.5}$$

The group is isomorphic to the group O_{24} of orientation-preserving symmetries of the cube (Arnold & Korkina, 1983; Arnold, 1984; Gilbert, 1992). For example an element such as a of order 4 corresponds to a $\pi/2$ rotation about the centre of a face while an element such as d of

order 3 is a $2\pi/3$ rotation about a diagonal. However in the case of the ABC flow symmetries, the translations are crucial also: just as it is a rotation and a translation that preserves the form of a helix as a curve in space, so too it is for the helical waves that make up the ABC flow. We shall see however that when fields are represented in Fourier space the translations become phase shifts so that the link with rotations and symmetries of a cube is somewhat clearer: it is a cube of wave-vectors that is thus transformed.

It is important to note that the action of each symmetry on a vector field such as $\boldsymbol{u}$, $\boldsymbol{b}$ or $\boldsymbol{v}$ involves not only transferring a vector from point to point, but also rotating it appropriately using the Jacobian of the transformation. Explicitly, for any transformation $\mathsf{g} \in G$, the action of g is to map any 2π-periodic vector field $\boldsymbol{b}$ to $\mathsf{g}\boldsymbol{b}$ with

$$(\mathsf{g}\boldsymbol{b})(\boldsymbol{r}) = \boldsymbol{J}_{\mathsf{g}}\, \boldsymbol{b}(\mathsf{g}^{-1}\boldsymbol{r}), \tag{2.6}$$

where $\boldsymbol{J}_{\mathsf{g}}$ is the Jacobian of the transformation g. This is familiar as frozen-field evolution under the rotational and translational motion needed to effect g. Note that for a 2π-periodic scalar field ϕ no Jacobian is needed, with $(\mathsf{g}\phi)(\boldsymbol{r}) = \phi(\mathsf{g}^{-1}\boldsymbol{r})$.

3 Representations

We are interested in solving (2.2) or (2.4) as an eigenvalue problem by setting

$$\boldsymbol{b} = \tilde{\boldsymbol{b}}(x,y,z)e^{\lambda t}, \quad \boldsymbol{v} = \tilde{\boldsymbol{v}}(x,y,z)e^{\lambda t}, \tag{3.1}$$

and seeking growth rates and frequencies of magnetic or velocity fields, together with their structure in physical space. We wish to exploit the symmetries of the ABC flow both to reduce the computational effort of the eigenvalue problem and also to investigate branches possessing distinct symmetries. This is common in many problems in the physical sciences (see, e.g., Hamermesh, 1962). The use of symmetry is familiar in straightforward cases; for example we can consider quadrupole and dipole symmetry for a dynamo in a sphere with reflection symmetry about the equator, the appropriate symmetry group being $\mathbb{Z}_2$. Any field can then be broken up into a quadrupole component and a dipole component, by adding or subtracting the reflected field. Such fields then evolve independently provided the evolution equation is linear and preserves the symmetry, and in this case there are separate eigenvalue problems with distinct branches of solutions. In the nonlinear regime there can then be symmetry breaking and mixed mode solutions, but that is not possible in the linear approximation.

3.1 Example of D_8: symmetries of a square

For readers who are not familiar with the generalisation to more complicated groups, and because the full group G in (2.5) is hard to visualise in three dimensions, we briefly explain the idea using the symmetry group D_8 of a square. We take the square to be centred at the origin with sides parallel to the x and y axes, depicted in figure 1(a). D_8 is generated by an anti-clockwise rotation r of $\pi/2$ about the origin and a reflection s in the x-axis,

$$\mathsf{r}(x,y) = (-y,x), \quad \mathsf{s}(x,y) = (x,-y), \tag{3.2}$$

and contains the elements $\{\mathsf{i}, \mathsf{r}, \mathsf{r}^2, \mathsf{r}^3, \mathsf{s}, \mathsf{rs}, \mathsf{r}^2\mathsf{s}, \mathsf{r}^3\mathsf{s}\}$. with $\mathsf{r}^4 = \mathsf{s}^2 = \mathsf{i}$ and $\mathsf{rs} = \mathsf{sr}^{-1}$.

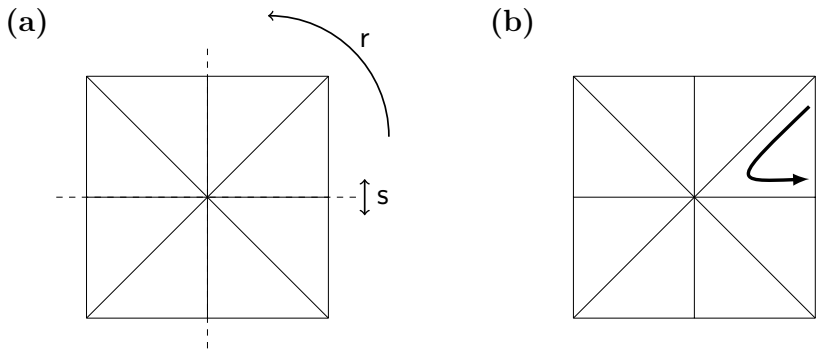

Fig. 1. Shown are (a) the geometry for a square with symmetry group D_8, and (b) a magnetic field $\boldsymbol{b}$ confined to one eighth of the square.

Suppose we start with a general magnetic field $\boldsymbol{b}(\boldsymbol{r})$. Then we may map it with each element $\mathsf{g} \in G$ to obtain 8 linearly independent magnetic fields, spanning a vector space W,

$$W = \mathrm{span}\{\boldsymbol{b}, \mathsf{r}\boldsymbol{b}, \mathsf{r}^2\boldsymbol{b}, \mathsf{r}^3\boldsymbol{b}, \mathsf{s}\boldsymbol{b}, \mathsf{rs}\boldsymbol{b}, \mathsf{r}^2\mathsf{s}\boldsymbol{b}, \mathsf{r}^3\mathsf{s}\boldsymbol{b}\}. \tag{3.3}$$

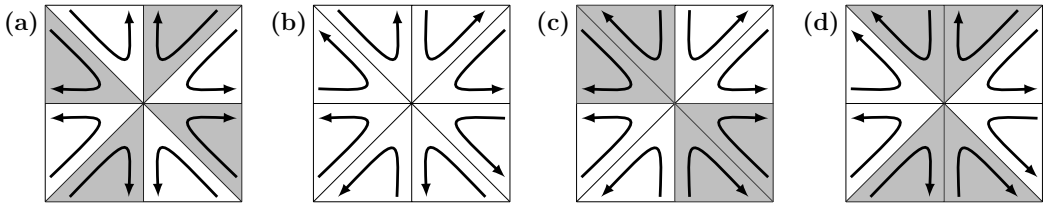

Fig. 2. Fields for representations I–IV: (a) $\boldsymbol{b}^{\mathrm{I}}$, (b) $\boldsymbol{b}^{\mathrm{II}}$, (c) $\boldsymbol{b}^{\mathrm{III}}$, and (d) $\boldsymbol{b}^{\mathrm{IV}}$.

A convenient way to visualise this is to consider a magnetic field depicted schematically in figure 1(b) which is confined to one-eighth of the square and has a anti-clockwise, or positive, sense. Then each transformation in G maps the field to a distinct eighth of the square and these fields are all plainly linearly independent. Note that under a reflection g, the resulting field $\mathsf{g}\boldsymbol{b}$ has a clockwise or negative sense. If we now seek single combinations of these eight fields that transform simply under group elements, we find we have four of these, labelled I–IV,

$$\boldsymbol{b}^{\mathrm{I}} = \boldsymbol{b} + \mathsf{r}\boldsymbol{b} + \mathsf{r}^2\boldsymbol{b} + \mathsf{r}^3\boldsymbol{b} + \mathsf{s}\boldsymbol{b} + \mathsf{rs}\boldsymbol{b} + \mathsf{r}^2\mathsf{s}\boldsymbol{b} + \mathsf{r}^3\mathsf{s}\boldsymbol{b}, \tag{3.4}$$

$$\boldsymbol{b}^{\mathrm{II}} = \boldsymbol{b} + \mathsf{r}\boldsymbol{b} + \mathsf{r}^2\boldsymbol{b} + \mathsf{r}^3\boldsymbol{b} - \mathsf{s}\boldsymbol{b} - \mathsf{rs}\boldsymbol{b} - \mathsf{r}^2\mathsf{s}\boldsymbol{b} - \mathsf{r}^3\mathsf{s}\boldsymbol{b}, \tag{3.5}$$

$$\boldsymbol{b}^{\mathrm{III}} = \boldsymbol{b} - \mathsf{r}\boldsymbol{b} + \mathsf{r}^2\boldsymbol{b} - \mathsf{r}^3\boldsymbol{b} + \mathsf{s}\boldsymbol{b} - \mathsf{rs}\boldsymbol{b} + \mathsf{r}^2\mathsf{s}\boldsymbol{b} - \mathsf{r}^3\mathsf{s}\boldsymbol{b}, \tag{3.6}$$

$$\boldsymbol{b}^{\mathrm{IV}} = \boldsymbol{b} - \mathsf{r}\boldsymbol{b} + \mathsf{r}^2\boldsymbol{b} - \mathsf{r}^3\boldsymbol{b} - \mathsf{s}\boldsymbol{b} + \mathsf{rs}\boldsymbol{b} - \mathsf{r}^2\mathsf{s}\boldsymbol{b} + \mathsf{r}^3\mathsf{s}\boldsymbol{b}. \tag{3.7}$$

These transform under any group element $\mathsf{g} \in G$ via multiplication through ± 1, that is

$$\mathsf{g}\boldsymbol{b}^{\alpha} = M^{\alpha}(\mathsf{g})\boldsymbol{b}^{\alpha} \tag{3.8}$$

where α labels the representation I–IV. For a given α the set of $M^{\alpha}(\mathsf{g})$ for $\mathsf{g} \in G$ is called an irreducible representation of the group G. For example for representation II we have

$$M^{\mathrm{II}}(\mathsf{i}) = M^{\mathrm{II}}(\mathsf{r}) = M^{\mathrm{II}}(\mathsf{r}^2) = M^{\mathrm{II}}(\mathsf{r}^3) = 1, \tag{3.9}$$

$$M^{\mathrm{II}}(\mathsf{s}) = M^{\mathrm{II}}(\mathsf{rs}) = M^{\mathrm{II}}(\mathsf{r}^2\mathsf{s}) = M^{\mathrm{II}}(\mathsf{r}^3\mathsf{s}) = -1, \tag{3.10}$$

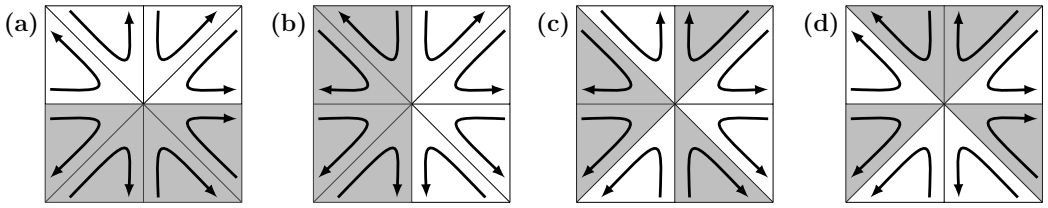

Fig. 3. Fields for representation V: (a) $\boldsymbol{b}_1^{\mathrm{V}a}$, (b) $\boldsymbol{b}_2^{\mathrm{V}a}$, (c) $\boldsymbol{b}_1^{\mathrm{V}b}$, and (d) $\boldsymbol{b}_2^{\mathrm{V}b}$.

while for representation I all the values are $M^{\mathrm{I}}(\mathsf{g}) = 1$. Plainly we have that

$$M^{\alpha}(\mathsf{g})M^{\alpha}(\mathsf{h}) = M^{\alpha}(\mathsf{gh}) \tag{3.11}$$

for any elements g and h in the group G. The values of the $M^{\alpha}(\mathsf{g})$ for $\mathsf{g} \in G$ can be read straight from the character table, table 1, for representations I–IV. Given the initial field $\boldsymbol{b}$ shown in figure 1(b) the four fields $\boldsymbol{b}^{\mathrm{I}}$ to $\boldsymbol{b}^{\mathrm{IV}}$ are seen schematically in figure 2. We have shaded where the field has a negative sense.

Table 1
Character table for the group D_8. Entries give the character, that is the trace of the matrix $\boldsymbol{M}^{\alpha}(\mathsf{g})$, for each transformation g and irreducible representation α from I–V.

	$\{\mathsf{i}\}$	$\{\mathsf{r}, \mathsf{r}^3\}$	$\{\mathsf{r}^2\}$	$\{\mathsf{s}, \mathsf{r}^2\mathsf{s}\}$	$\{\mathsf{rs}, \mathsf{r}^3\mathsf{s}\}$
I	1	1	1	1	1
II	1	1	1	−1	−1
III	1	−1	1	1	−1
IV	1	−1	1	−1	1
V	2	0	−2	0	0

The four fields in (3.4–3.7) transform by multiplication by ± 1 under transformations of the square, but cannot span the full eight-dimensional vector space of fields W in (3.3). It is clear for example that they do not include the possibility of a non-zero mean field in the system, as under the $\pi/2$ rotation r such a field could not transform to ± 1 times itself. In fact the set of fields (3.4–3.7) exhaust the one-dimensional representations of the group G, and the next best we can do is to define pairs of fields in the two-dimensional representations,

$$\begin{aligned}
\boldsymbol{b}_1^{\mathrm{Va}} &= \boldsymbol{b} + \mathsf{r}\boldsymbol{b} - \mathsf{r}^2\boldsymbol{b} - \mathsf{r}^3\boldsymbol{b} + \mathsf{s}\boldsymbol{b} - \mathsf{rs}\boldsymbol{b} - \mathsf{r}^2\mathsf{s}\boldsymbol{b} + \mathsf{r}^3\mathsf{s}\boldsymbol{b}, \\
\boldsymbol{b}_2^{\mathrm{Va}} &= \boldsymbol{b} - \mathsf{r}\boldsymbol{b} - \mathsf{r}^2\boldsymbol{b} + \mathsf{r}^3\boldsymbol{b} - \mathsf{s}\boldsymbol{b} - \mathsf{rs}\boldsymbol{b} + \mathsf{r}^2\mathsf{s}\boldsymbol{b} + \mathsf{r}^3\mathsf{s}\boldsymbol{b},
\end{aligned} \tag{3.12}$$

and

$$\begin{aligned}
\boldsymbol{b}_1^{\mathrm{Vb}} &= \boldsymbol{b} + \mathsf{r}\boldsymbol{b} - \mathsf{r}^2\boldsymbol{b} - \mathsf{r}^3\boldsymbol{b} - \mathsf{s}\boldsymbol{b} + \mathsf{rs}\boldsymbol{b} + \mathsf{r}^2\mathsf{s}\boldsymbol{b} - \mathsf{r}^3\mathsf{s}\boldsymbol{b}, \\
\boldsymbol{b}_2^{\mathrm{Vb}} &= \boldsymbol{b} - \mathsf{r}\boldsymbol{b} - \mathsf{r}^2\boldsymbol{b} + \mathsf{r}^3\boldsymbol{b} + \mathsf{s}\boldsymbol{b} + \mathsf{rs}\boldsymbol{b} - \mathsf{r}^2\mathsf{s}\boldsymbol{b} - \mathsf{r}^3\mathsf{s}\boldsymbol{b}.
\end{aligned} \tag{3.13}$$

Note that subscripts label different fields, not their Cartesian components. These four fields are depicted in figure 3.

Focusing on the first pair of fields (3.12) shown in figure 3(a,b), we have

$$\mathsf{r}\boldsymbol{b}_1^{\mathrm{Va}} = -\boldsymbol{b}_2^{\mathrm{Va}}, \quad \mathsf{r}\boldsymbol{b}_2^{\mathrm{Va}} = \boldsymbol{b}_1^{\mathrm{Va}}, \quad \mathsf{s}\boldsymbol{b}_1^{\mathrm{Va}} = \boldsymbol{b}_1^{\mathrm{Va}}, \quad \mathsf{s}\boldsymbol{b}_2^{\mathrm{Va}} = -\boldsymbol{b}_2^{\mathrm{Va}}, \tag{3.14}$$

and so now the action of the group elements is given by 2×2 matrices defined by

$$\boldsymbol{M}^{\mathrm{Va}}(\mathsf{r}) = \begin{pmatrix} 0 & -1 \\ 1 & 0 \end{pmatrix}, \quad \boldsymbol{M}^{\mathrm{Va}}(\mathsf{s}) = \begin{pmatrix} 1 & 0 \\ 0 & -1 \end{pmatrix}, \tag{3.15}$$

with

$$\mathsf{g}\boldsymbol{b}_i^\alpha = \sum_j M_{ij}^\alpha(\mathsf{g})\, \boldsymbol{b}_j^\alpha, \tag{3.16}$$

where the label α corresponds to the label 'Va'. The matrices for the remaining transformations follow by matrix multiplication, using the requirement that (3.11) hold, now as a matrix equation. Note that the fields $\boldsymbol{b}_1^{\mathrm{Va}}$ and $\boldsymbol{b}_2^{\mathrm{Va}}$ allow the possibility of a mean field in the y and x directions respectively. These two fields give a two-dimensional irreducible representation.

The second pair of fields, in (3.13), corresponds to another two-dimensional irreducible representation 'Vb' isomorphic to Va, and we omit the details. All the representations, I, II, III, IV and two copies of V, span the vector space W in (3.3) and any field $\boldsymbol{b}$ can be decomposed into components in each of these spaces as above with

$$8\boldsymbol{b} = \boldsymbol{b}^{\mathrm{I}} + \boldsymbol{b}^{\mathrm{II}} + \boldsymbol{b}^{\mathrm{III}} + \boldsymbol{b}^{\mathrm{IV}} + \boldsymbol{b}_1^{\mathrm{Va}} + \boldsymbol{b}_2^{\mathrm{Va}} + \boldsymbol{b}_1^{\mathrm{Vb}} + \boldsymbol{b}_2^{\mathrm{Vb}}. \tag{3.17}$$

Some comments are in order. We have four one-dimensional irreducible representations I–IV, in which the action on the corresponding field is multiplication by 1×1 matrices (see (3.8)). We have two copies of what is essentially the same two-dimensional representation V in which the action is on pairs of fields through multiplication by 2×2 matrices. The actual matrices are not unique under a change of basis, though we have provided a rational choice with $M^\alpha(\mathsf{g}) = \boldsymbol{J}_{\mathsf{g}}$. The form of the fields in (3.12,3.13) are dependent on this (somewhat arbitrary) choice. Only the traces of the matrices are invariant, and these are given in the character table, table 1. As the matrix for the group identity operation i is always the identity matrix, this column gives the dimension of the irreducible representation.

Going back to the basis of fields of W given in (3.3), the action of an element $\mathsf{g} \in G$ is simply to permute these fields and so give rise to a (reducible) representation with 8×8 matrices $\boldsymbol{M}(\mathsf{g})$ having a permutation form (i.e. a single entry of 1 per column and row). Representation theory can be seen as a way to choose a basis (of magnetic fields here) so as far as possible to diagonalise simultaneously the matrices for all the $\mathsf{g} \in G$. In our example of D_8, under the basis in (3.7,3.12,3.13) the 8×8 matrix for each g takes a block diagonal form

$$\boldsymbol{M}(\mathsf{g}) = \begin{pmatrix} M^{\mathrm{I}}(\mathsf{g}) & 0 & 0 & 0 & \cdots & & \\ 0 & M^{\mathrm{II}}(\mathsf{g}) & 0 & 0 & & & \\ 0 & 0 & M^{\mathrm{III}}(\mathsf{g}) & 0 & & & \vdots \\ 0 & 0 & 0 & M^{\mathrm{IV}}(\mathsf{g}) & \ddots & & \\ \vdots & & & \ddots & \boldsymbol{M}^{\mathrm{Va}}(\mathsf{g}) & \boldsymbol{0} & \\ & & \cdots & & \boldsymbol{0} & \boldsymbol{M}^{\mathrm{Vb}}(\mathsf{g}) & \end{pmatrix}. \tag{3.18}$$

Any linear problem that respects the symmetries can be considered in each of the six subspaces independently, in particular any linear eigenvalue problem. Thus instead of solving

the full problem, we have five distinct reduced problems (we need only consider one copy of representation V), each with its own set of eigenvalues.

Finally, we note that it is not necessary to give the fields of each irreducible representation as they are displayed in (3.4–3.7, 3.12, 3.13) for D_8. We have done so simply to demonstrate how these fields relate to those of the vector space W in this example. For larger groups G this becomes an increasingly arduous and uninteresting task. The key information is how each of these fields is transformed by the elements of G, which simply requires knowing matrices $\boldsymbol{M}^\alpha(\mathsf{g})$ for each irreducible representation α.

3.2 Representations for the ABC flows

Having completed our brief tour of representation theory with the example of D_8, we now return to the problem in hand and discuss the ABC flows and representations under the group G with elements given in (2.5) (Arnold & Korkina, 1983; Arnold, 1984; Gilbert, 1992). Given a sufficiently general magnetic field $\boldsymbol{b}$ we obtain a 24-dimensional vector space W spanned by the images $\mathsf{g}\boldsymbol{b}$ under the various symmetries.

Table 2
Character table for the group O_{24}. Entries give the character, that is the trace of the matrix $\boldsymbol{M}^\alpha(\mathsf{g})$, for transformations g in the conjugacy classes (3.19) and irreducible representations α from I–V.

	E	C_3	C_4^2	C_2	C_4
I	1	1	1	1	1
II	1	1	1	−1	−1
III	2	−1	2	0	0
IV	3	0	−1	1	−1
V	3	0	−1	−1	1

Rather than writing down a decomposition of this space explicitly, we start by giving the character table for G (i.e. that of the orientation-preserving symmetries of a cube) in table 2. Here the elements are grouped into conjugacy classes with

$$\begin{aligned} E &= \{\mathsf{i}\}, \quad C_4 = \{\mathsf{a}, \mathsf{a}^3, \mathsf{b}, \mathsf{b}^3, \mathsf{c}, \mathsf{c}^3\}, \quad C_4^2 = \{\mathsf{a}^2, \mathsf{b}^2, \mathsf{c}^2\}, \\ C_3 &= \{\mathsf{d}, \mathsf{d}^2, \mathsf{e}, \mathsf{e}^2, \mathsf{f}, \mathsf{f}^2, \mathsf{g}, \mathsf{g}^2\}, \quad C_2 = \{\mathsf{h}, \mathsf{j}, \mathsf{k}, \mathsf{l}, \mathsf{m}, \mathsf{n}\} \end{aligned} \tag{3.19}$$

(see Hamermesh (1962), for example). From the first column of the table we have a pair of one-dimensional representations I and II in which the field is multiplied by ± 1 under each symmetry operation. The values may be read from the character table. Moving to the bottom of the table, there is a pair of three-dimensional representations IV and V. These will occur three times in a decomposition of the action of the group on a general magnetic field, but we

need only consider one copy of each. Key matrices we will find useful are

$$\boldsymbol{M}^{\alpha}(\mathsf{b}) = \pm\begin{pmatrix} -1 & 0 & 0 \\ 0 & 0 & 1 \\ 0 & -1 & 0 \end{pmatrix}, \quad \boldsymbol{M}^{\alpha}(\mathsf{b}^3) = \pm\begin{pmatrix} -1 & 0 & 0 \\ 0 & 0 & -1 \\ 0 & 1 & 0 \end{pmatrix},$$
$$\boldsymbol{M}^{\alpha}(\mathsf{d}) = \begin{pmatrix} 0 & 0 & 1 \\ 1 & 0 & 0 \\ 0 & 1 & 0 \end{pmatrix}, \quad \boldsymbol{M}^{\alpha}(\mathsf{d}^2) = \begin{pmatrix} 0 & 1 & 0 \\ 0 & 0 & 1 \\ 1 & 0 & 0 \end{pmatrix}, \tag{3.20}$$

and a full set may be found in Appendix A. Here for representation α as IV we take the upper sign, and for V we take the lower sign. Note that in representation V, the matrices $\boldsymbol{M}^{\mathrm{V}}(\mathsf{g})$ correspond to the Jacobians of the transformation in (2.5) for the corresponding group element g. Representation IV can be considered as the tensor product of V and II (Arnold, 1984).

Somewhat less intuitive, in the middle of the table, is a two-dimensional representation III. This is given in full in Appendix A and here we note that

$$\boldsymbol{M}^{\mathrm{III}}(\mathsf{b}) = \boldsymbol{M}^{\mathrm{III}}(\mathsf{b}^3) = \frac{1}{2}\begin{pmatrix} 1 & -\sqrt{3} \\ -\sqrt{3} & -1 \end{pmatrix},$$
$$\boldsymbol{M}^{\mathrm{III}}(\mathsf{d}) = \frac{1}{2}\begin{pmatrix} -1 & \sqrt{3} \\ -\sqrt{3} & -1 \end{pmatrix}, \quad \boldsymbol{M}^{\mathrm{III}}(\mathsf{d}^2) = \frac{1}{2}\begin{pmatrix} -1 & -\sqrt{3} \\ \sqrt{3} & -1 \end{pmatrix}. \tag{3.21}$$

Although we do not decompose the 24-dimensional space W generated by a single magnetic field under the action of symmetries in G (as we did for D_8 in section 3.1), we note that this contains one copy of representations I and II, two copies of III, and three copies of each of IV and V, and these span W with $1^2 + 1^2 + 2^2 + 3^2 + 3^2 = 24$, the order of G as required (e.g., Hamermesh, 1962).

4 Numerical methods

Our aim is to find eigenvalues and magnetic field eigenfunctions corresponding to each representation. We consider magnetic fields with the usual Fourier decomposition

$$\boldsymbol{b} = \sum_{l,m,n} \boldsymbol{b}_{l,m,n}(t)\, e^{ilx+imy+inz}, \qquad \boldsymbol{b}_{l,m,n} = (X_{l,m,n}, Y_{l,m,n}, Z_{l,m,n}). \tag{4.1}$$

We also have the Hermitian symmetry property,

$$\boldsymbol{b}_{l,m,n} = \boldsymbol{b}^*_{-l,-m,-n}. \tag{4.2}$$

Numerically the values of l, m and n are limited by the maximum resolution N with $|l|, |m|, |n| \leq N$ and the zero mode (which would correspond to a constant mean field) is always set to zero.

4.1 Time stepping

We first consider solving the problem without imposing any symmetries. As discussed in Galloway & Frisch (1986) the great advantage of the ABC flow is that the terms involving $\boldsymbol{u}$ and $\boldsymbol{b}$ couple neighbouring modes in Fourier space, and so a purely spectral code is appropriate, there being no need to take Fourier transforms to and from real space, except when the resulting magnetic fields are to be visualised.

For the advective and stretching terms we have adopted a three-step Adams–Bashforth scheme as a balance between accuracy and speed. The diffusive terms are integrated exactly and give exponential damping of each mode every time step. This scheme can be written analytically (and clumsily) for the x-component with time $t = j\Delta t$ as

$$X^{j+1}_{l,m,n} = E_{l,m,n}\left[X^{j}_{l,m,n} + \tfrac{1}{12}\Delta t\left(23\Lambda^{j}_{l,m,n} - 16E_{l,m,n}\Lambda^{j-1}_{l,m,n} + 5E^{2}_{l,m,n}\Lambda^{j-2}_{l,m,n}\right)\right], \tag{4.3}$$

where

$$E_{l,m,n} = \exp(-\varepsilon(l^2+m^2+n^2)\Delta t). \tag{4.4}$$

The advective and stretching terms at time step j are represented by $\Lambda^{j}_{l,m,m}$ for the x-component, and are given by

$$\begin{aligned} 2\Lambda^{j}_{l,m,n} = {} & im\left(Y^{j}_{l,m-1,n} + Y^{j}_{l,m+1,n}\right) - im\left(X^{j}_{l,m,n-1} + X^{j}_{l,m,n+1}\right) \\ & + m\left(Y^{j}_{l,m,n-1} - Y^{j}_{l,m,n+1}\right) - m\left(X^{j}_{l-1,m,n} - X^{j}_{l+1,m,n}\right) \\ & + in\left(Z^{j}_{l,m-1,n} + Z^{j}_{l,m+1,n}\right) - in\left(X^{j}_{l-1,m,n} + X^{j}_{l+1,m,n}\right) \\ & + n\left(Z^{j}_{l,m,n-1} - Z^{j}_{l,m,n+1}\right) - n\left(X^{j}_{l,m-1,n} - X^{j}_{l,m+1,n}\right). \end{aligned} \tag{4.5}$$

The y and z components of $\boldsymbol{b}_{l,m,n}$ are time stepped according to similar expressions. The time stepping for the fluid stability problem (2.4) is very similar, with a projection in spectral space used to incorporate the effect of the pressure term.

4.2 Reduced domain without Hermitian symmetry

We now consider the use of symmetries to reduce the scale of the numerical problem of finding ABC dynamo growth rates, and follow different eigenfunction branches. We work with the magnetic field written in the Fourier space decomposition (4.1) with $|l|, |m|, |n| \le N$, but in this section do not consider the imposition of Hermitian symmetry (4.2) (see the discussion of the Arnoldi solver below). In this case the key point is that given a magnetic field Fourier amplitude $\boldsymbol{b}_{l,m,n}$ for a general value of the wave number (l, m, n), each symmetry operation in (2.5) will give a distinct Fourier mode. For example the (l, m, n) modes of $\mathsf{b}\boldsymbol{b}$ and of $\mathsf{d}\boldsymbol{b}$ are given by

$$(\mathsf{b}\boldsymbol{b})_{l,m,n} = e^{i(l-m-n)\pi/2}\,\boldsymbol{J}_{\mathsf{b}}\,\boldsymbol{b}_{l,n,-m}, \quad (\mathsf{d}\boldsymbol{b})_{l,m,n} = \boldsymbol{J}_{\mathsf{d}}\,\boldsymbol{b}_{m,n,l}, \tag{4.6}$$

while for their inverses,

$$(\mathsf{b}^3\boldsymbol{b})_{l,m,n} = e^{i(-l+m-n)\pi/2}\,\boldsymbol{J}_{\mathsf{b}^3}\,\boldsymbol{b}_{l,-n,m}, \quad (\mathsf{d}^2\boldsymbol{b})_{l,m,n} = \boldsymbol{J}_{\mathsf{d}^2}\,\boldsymbol{b}_{n,l,m}. \tag{4.7}$$

For representations I and II the operation $\mathsf{d}\boldsymbol{b}$ gives the original field, while $\mathsf{b}\boldsymbol{b}$ gives ± 1 times

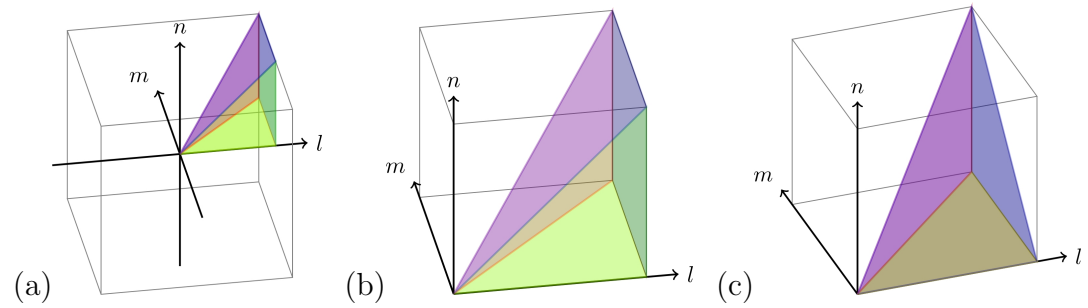

Fig. 4. Fundamental domain $\mathcal{G}_N$ (a) within the full cube of wave vectors, (b) a close up view of $\mathcal{G}_N$ and (c) a close up view of $\mathcal{H}_N$.

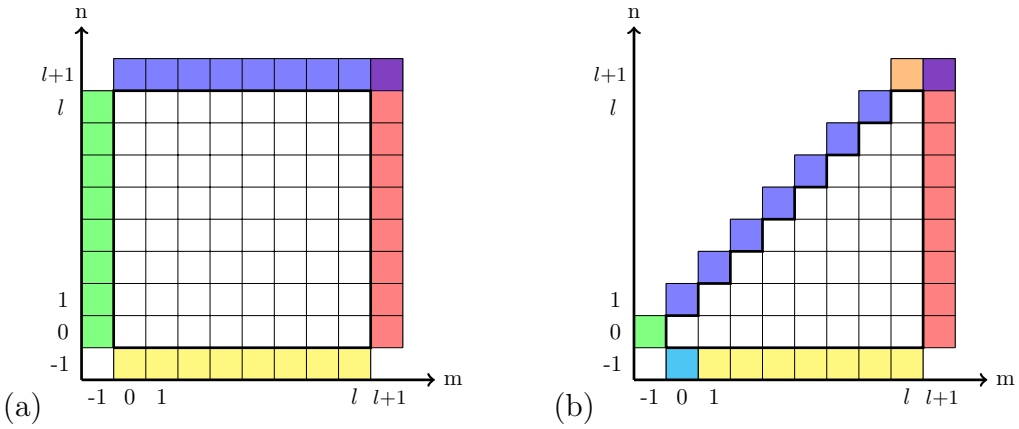

Fig. 5. A slice of constant l when (a) Hermitian symmetry is not imposed, and (b) when it is. Coloured (shaded) modes need to be filled in using the symmetries; different colours (shades) represent different transformations required to calculate mode values.

the field, with the upper sign for representation I and the lower for II,

$$\boldsymbol{b}_{l,m,n} = \pm e^{i(l-m-n)\pi/2}\, \boldsymbol{J}_{\mathsf{b}}\, \boldsymbol{b}_{l,n,-m}, \quad \boldsymbol{b}_{l,m,n} = \boldsymbol{J}_{\mathsf{d}}\, \boldsymbol{b}_{m,n,l}. \tag{4.8}$$

Applying this argument for all group symmetries we find that knowing $\boldsymbol{b}_{l,m,n}$ for a general mode (l, m, n) tells us the amplitude of 24 Fourier modes.

Thus we may reduce the size of the computational domain, in Fourier space, to the wedge indicated in figure 4(a,b). We call this the *fundamental domain* $\mathcal{G}_N$ which contains wave-vectors given by

$$\mathcal{G}_N = \{(l, m, n) : 1 \le l \le N, 0 \le m \le l, 0 \le n \le l\}. \tag{4.9}$$

Now we consider time stepping the Fourier mode amplitudes $\boldsymbol{b}_{l,m,n}$ with wave vectors in $\mathcal{G}_N$. As the evolution couples each wave vector to its 6 nearest neighbours, our procedure is to fill in the mode amplitudes around the edges of $\mathcal{G}_N$ using the symmetries, then to use the time stepping method outlined in section 4.1.

To explain this further, consider a *slice* of modes given by a constant value of $l \ge 1$ and m, n with $0 \le m, n \le l$. The modes we wish to time step are shown unshaded in figure 5(a) and the neighbouring ones that we need to fill in to take a step are shown shaded. Note that we need to fill in the corner mode $\boldsymbol{b}_{l,l+1,l+1}$ in slice l so that we can time step all the modes in slice $l + 1$. Given only the modes in the unshaded region, we can use appropriate choices of modes (l, m, n) in (4.8) to fill in the left and right columns of shaded modes for representations I and

II by

$$\boldsymbol{b}_{l,-1,n} = \pm e^{i(l+1-n)\pi/2}\, \boldsymbol{J}_{\mathsf{b}}\, \boldsymbol{b}_{l,n,1}, \quad \boldsymbol{b}_{l,l+1,n} = \boldsymbol{J}_{\mathsf{d}}\, \boldsymbol{b}_{l+1,n,l}, \tag{4.10}$$

which use modes in the fundamental domain on the right-hand side. Likewise we use b^3 and d^2 to fill in the rows of modes $\boldsymbol{b}_{l,m,-1}$ and $\boldsymbol{b}_{l,m,l+1}$ in terms of modes that lie in $\mathcal{G}_N$;

$$\boldsymbol{b}_{l,m,-1} = \pm e^{i(-l+m+1)\pi/2}\, \boldsymbol{J}_{\mathsf{b}^3}\, \boldsymbol{b}_{l,1,m}, \quad \boldsymbol{b}_{l,m,l+1} = \boldsymbol{J}_{\mathsf{d}^2}\, \boldsymbol{b}_{l+1,l,m}. \tag{4.11}$$

The procedure is a little more complicated for the two- and three-dimensional representations. Taking IV and V together, we now have three distinct fields $\boldsymbol{b}_1$, $\boldsymbol{b}_2$ and $\boldsymbol{b}_3$ to be stored on all modes in the fundamental domain $\mathcal{G}_N$. For time stepping, each of the three fields $\boldsymbol{b}_1$, $\boldsymbol{b}_2$,, $\boldsymbol{b}_3$ is again stepped on modes in $\mathcal{G}_N$. If we focus on a slice of $\mathcal{G}_N$ in figure 5(a) then for a time step, we again need to fill in the fields $\boldsymbol{b}_1$, $\boldsymbol{b}_2$, $\boldsymbol{b}_3$ for the shaded modes around the edges of the slice, and this is done by using symmetry properties of IV and V. When we apply a symmetry operation these three fields are mapped according to (3.16) with the representation matrices $\boldsymbol{M}^{\alpha}(\mathsf{g})$ given in (3.20). In addition when a symmetry operation is applied, the *components* of the field are premultiplied by $\boldsymbol{J}_{\mathsf{g}}$, with a phase shift.

We start with the trivial remark that $\boldsymbol{b} = \mathsf{b}^4\boldsymbol{b} = \mathsf{b}^3(\mathsf{b}\boldsymbol{b})$ and so use of the matrix in (3.20) for b^3 yields

$$\boldsymbol{b}_1 = \mp \mathsf{b}\boldsymbol{b}_1, \quad \boldsymbol{b}_2 = \mp \mathsf{b}\boldsymbol{b}_3, \quad \boldsymbol{b}_3 = \pm \mathsf{b}\boldsymbol{b}_2, \tag{4.12}$$

which with (4.6) gives the relationship, for any l, m, n,

$$\begin{aligned}
(\boldsymbol{b}_1)_{l,m,n} &= \mp e^{i(l-m-n)\pi/2}\, \boldsymbol{J}_{\mathsf{b}}\, (\boldsymbol{b}_1)_{l,n,-m}, \\
(\boldsymbol{b}_2)_{l,m,n} &= \mp e^{i(l-m-n)\pi/2}\, \boldsymbol{J}_{\mathsf{b}}\, (\boldsymbol{b}_3)_{l,n,-m}, \\
(\boldsymbol{b}_3)_{l,m,n} &= \pm e^{i(l-m-n)\pi/2}\, \boldsymbol{J}_{\mathsf{b}}\, (\boldsymbol{b}_2)_{l,n,-m}.
\end{aligned} \tag{4.13}$$

This holds for any modes in a set of fields in representation IV (upper sign) or V (lower sign). Similar for the rotation d we have that $\boldsymbol{b} = \mathsf{d}^2(\mathsf{d}\boldsymbol{b})$ and so

$$\boldsymbol{b}_1 = \mathsf{d}\boldsymbol{b}_2, \quad \boldsymbol{b}_2 = \mathsf{d}\boldsymbol{b}_3, \quad \boldsymbol{b}_3 = \mathsf{d}\boldsymbol{b}_1, \tag{4.14}$$

which with (4.6) yields

$$(\boldsymbol{b}_1)_{l,m,n} = \boldsymbol{J}_{\mathsf{d}}\, (\boldsymbol{b}_2)_{m,n,l}, \ (\boldsymbol{b}_2)_{l,m,n} = \boldsymbol{J}_{\mathsf{d}}\, (\boldsymbol{b}_3)_{m,n,l}, \ (\boldsymbol{b}_3)_{l,m,n} = \boldsymbol{J}_{\mathsf{d}}\, (\boldsymbol{b}_1)_{m,n,l}. \tag{4.15}$$

These transformations interchange the three fields and their components with appropriate phase shifts (from the translations in real space) and changes of sign. Use of these transformations enables us to fill in the left and right columns of modes in figure 5(a) by taking the choices of indices used in (4.10) and (4.11). Similar b^3 and d^2 can be used to fill in the top and bottom rows. We omit the details which are straightforward.

The picture for representation III is similar but less intuitive. Nonetheless we can proceed in the same fashion, with two fields $\boldsymbol{b}_1$ and $\boldsymbol{b}_2$ represented in the fundamental domain, and for the transformation b the analogous equation to (4.12) is

$$2\boldsymbol{b}_1 = \mathsf{b}\boldsymbol{b}_1 - \sqrt{3}\mathsf{b}\boldsymbol{b}_2, \quad 2\boldsymbol{b}_2 = -\sqrt{3}\mathsf{b}\boldsymbol{b}_1 - \mathsf{b}\boldsymbol{b}_2, \tag{4.16}$$

and so

$$2(\boldsymbol{b}_1)_{l,m,n} = e^{i(l-m-n)\pi/2}\,\boldsymbol{J}_{\mathsf{b}}\,[(\boldsymbol{b}_1)_{l,n,-m} - \sqrt{3}(\boldsymbol{b}_2)_{l,n,-m}],$$
$$2(\boldsymbol{b}_2)_{l,m,n} = e^{i(l-m-n)\pi/2}\,\boldsymbol{J}_{\mathsf{b}}\,[-\sqrt{3}(\boldsymbol{b}_1)_{l,n,-m} - (\boldsymbol{b}_2)_{l,n,-m}], \tag{4.17}$$

while for the transformation d the equivalent of (4.14) is

$$2\boldsymbol{b}_1 = -\mathsf{d}\boldsymbol{b}_1 - \sqrt{3}\mathsf{d}\boldsymbol{b}_2, \quad 2\boldsymbol{b}_2 = \sqrt{3}\mathsf{d}\boldsymbol{b}_1 - \mathsf{d}\boldsymbol{b}_2, \tag{4.18}$$

giving

$$2(\boldsymbol{b}_1)_{l,m,n} = \boldsymbol{J}_{\mathsf{d}}\,[-(\boldsymbol{b}_1)_{m,n,l} - \sqrt{3}(\boldsymbol{b}_2)_{m,n,l}],$$
$$2(\boldsymbol{b}_2)_{l,m,n} = \boldsymbol{J}_{\mathsf{d}}\,[\sqrt{3}(\boldsymbol{b}_1)_{m,n,l} - (\boldsymbol{b}_2)_{m,n,l}]. \tag{4.19}$$

Here the magnetic field components are mapped according to the Jacobians $\boldsymbol{J}_{\mathsf{g}}$ whereas the two fields are combined using the 2×2 matrices that give representation III. Again once (4.17,4.19) are established, they may be used to fill in the amplitudes of the shaded modes in the slice in figure 5(a) by appropriate choices of the mode (l,m,n) as we did for representations I and II in (4.10, 4.11).

4.3 Reduced domain with Hermitian symmetry

In simulating ABC dynamos through time stepping in previous studies, it has been natural to exploit the Hermitian symmetry (4.2) to use half the Fourier modes in a traditional truncation of (4.1), for example in place of the full cube $|l|,|m|,|n| \le N$, to use the half-cube $0 \le l,|m|,|n| \le N$, thus reducing the computer time required by a factor of two. We can also use Hermitian symmetry to halve our fundamental domain $\mathcal{G}_N$ and to time step modes in

$$\mathcal{H}_N = \{(l,m,n) : 1 \le l \le N, 0 \le m \le l, 0 \le n \le m\}. \tag{4.20}$$

This is shown in 4(c) and a slice of constant l is depicted in figure 5(b). We only sketch the procedure.

To time step the unshaded modes in $\mathcal{H}_N$ depicted in figure 4(c), we need to use various transformations, some making the additional use of the Hermitian symmetry (4.2) to fill in the shaded modes. For example, without Hermitian symmetry, the modes $\boldsymbol{b}_{l,m,n}$ and $\boldsymbol{b}_{l,n,m}$ cannot be related but with this symmetry and the transformation l, we have

$$(\mathsf{l}\boldsymbol{b})_{l,m,n} = e^{i(l+m+n)\pi/2}\,\boldsymbol{J}_{\mathsf{l}}\,\boldsymbol{b}_{-l,-n,-m} = e^{i(l+m+n)\pi/2}\,\boldsymbol{J}_{\mathsf{l}}\,\boldsymbol{b}^*_{l,n,m}. \tag{4.21}$$

There are several sets of modes, each requiring a specific transformation to calculate values from modes lying within $\mathcal{H}_N$; see again figure 5(b). We indicate briefly how to do this for each set. Firstly, the diagonal shaded modes $\boldsymbol{b}_{l,m,m+1}$ with $0 \le m \le l-1$ are filled in using (4.21) with appropriate indices,

$$(\mathsf{l}\boldsymbol{b})_{l,m,m+1} = e^{i(l+2m+1)\pi/2}\,\boldsymbol{J}_{\mathsf{l}}\,\boldsymbol{b}^*_{l,m+1,m}. \tag{4.22}$$

The bottom row of modes, $\boldsymbol{b}_{l,m,-1}$, for $1 \le m \le l$ is calculated using a^2 and a conjugation with

$$(\mathsf{a}^2\boldsymbol{b})_{l,m,-1} = e^{i(-m-1)\pi}\,\boldsymbol{J}_{\mathsf{a}^2}\,\boldsymbol{b}^*_{l,m,1}. \tag{4.23}$$

The right-hand set of modes, $\boldsymbol{b}_{l,l+1,n}$ for $0 \le n \le l$, are found through n and a conjugation as

$$(\mathsf{n}\boldsymbol{b})_{l,l+1,n} = e^{i(2l+n+1)\pi/2}\, \boldsymbol{J}_{\mathsf{n}}\, \boldsymbol{b}^*_{l+1,l,n}. \tag{4.24}$$

For the bottom left corner of the triangle we use

$$(\mathsf{b}^2\boldsymbol{b})_{l,-1,0} = e^{il\pi}\, \boldsymbol{J}_{\mathsf{b}^2}\, \boldsymbol{b}_{l,1,0}, \quad (\mathsf{b}^3\boldsymbol{b})_{l,0,-1} = e^{i(-l+1)\pi/2}\, \boldsymbol{J}_{\mathsf{b}^3}\, \boldsymbol{b}_{l,1,0}, \tag{4.25}$$

while for the top right corner we have

$$(\mathsf{d}^2\boldsymbol{b})_{l,l,l+1} = \boldsymbol{J}_{\mathsf{d}^2}\, \boldsymbol{b}_{l+1,l,l}, \quad (\mathsf{d}\boldsymbol{b})_{l,l+1,l+1} = \boldsymbol{J}_{\mathsf{d}}\, \boldsymbol{b}_{l+1,l+1,l}. \tag{4.26}$$

4.4 Comparison between time stepping and an Arnoldi eigenvalue solver

The above sections give a variety of methods of handling the time stepping: namely using the half cube of Fourier modes with Hermitian symmetry, or using the fundamental domains $\mathcal{G}_N$ or $\mathcal{H}_N$. This enables rigorous testing of the various codes that were developed. While the full code will always, in due course, select the fastest growing mode, over moderate time scales it may be used as a test for magnetic fields in each representation with careful choice of initial conditions having the appropriate symmetry properties. The symmetries apply equally in simulations of the dynamo problem (2.2) and the fluid stability problem (2.4). Figure 6 shows the typical output showing the square root of energy against time, and the overall slope of the curve gives the real growth rate. The frequency can be extracted from the period of the oscillatory component.

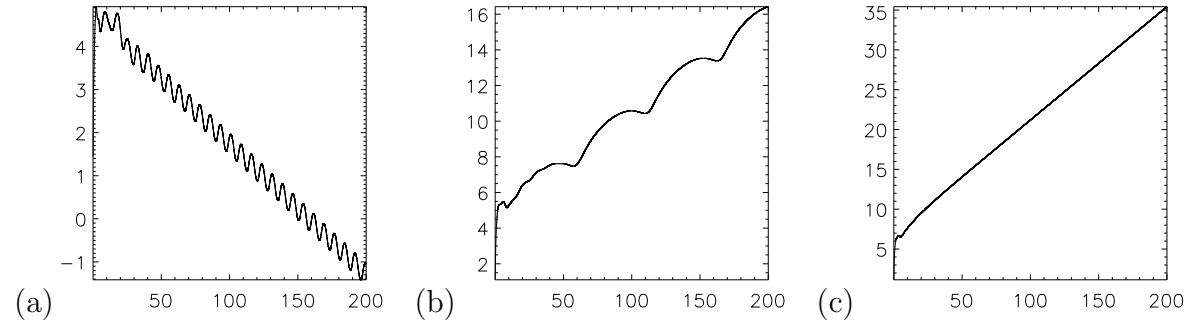

Fig. 6. Magnetic energy profiles for (a) class II, $R_m = 100$, (b) class V, $R_m = 100$, and (c) class V, $R_m = 250$

Note that for time stepping the saving in computer time over a full (Hermitian) code is a factor of 1/24 for (Hermitian) codes specific to the one-dimensional representations I and II, 1/12 for III and 1/8 for IV and V (in the limit of large N, in which the overhead in mode copying is a subdominant computational cost). Thus, for example, all solution branches could be followed with a net saving of 10/24 in terms of computer time. The savings in memory usage are less clear cut, as we stored each field $\boldsymbol{b}_j$ in the fundamental domain $\mathcal{H}_N$ or $\mathcal{G}_N$ in a three-dimensional cube with subscripts between -1 and N for speed and ease of programming. Of this array only about 1/6 was in use for the $\mathcal{H}_N$ code, for large N. We used two such cubes for representation III and three for IV or V. Memory could be used more efficiently; for example one could store the modes for the three fields $\boldsymbol{b}_1$, $\boldsymbol{b}_2$, $\boldsymbol{b}_3$ in the same cube for representations IV and V. However we did not do this, and note that computer time, rather than memory, is the main limitation for these codes.

There are a number of advantages to time stepping. Codes are easily run and may be parallelised given the local interactions between modes in spectral space. On the other hand determining the real and imaginary part of an eigenvalue can be time consuming near to a mode crossing, when two complex eigenvalues are about coalesce on the real line, giving a low frequency oscillation. Indeed the difficulty in determining growth rates at such an eigenvalue coalescence is the origin of considerable uncertainty in growth rates in the second window of dynamo action in the study of Galloway & Frisch (1986), recently resolved in Bouya & Dormy (2013).

An alternative method which we implemented and which has some advantages is to use a sparse eigenvalue solver. We chose to use ARPACK, available within the NAG scientific library, which solves problems of the form $A\boldsymbol{w} = \lambda\boldsymbol{w}$, using an Arnoldi method; see Trefethen & Bau (1997). The user code is required to return $A\boldsymbol{w}$ when the ARPACK subroutine supplies any vector $\boldsymbol{w}$. Ideally the user should also be able to supply $(A-\sigma)^{-1}\boldsymbol{w}$ when the routine supplies $\boldsymbol{w}$ and σ, but in our problem it is not realistic to invert the resulting linear system. The routine can determine eigenvalues λ of greatest or least magnitude, real part, or imaginary part; we require greatest real part. We consider the dynamo (and similarly the fluid stability) problem as a matrix eigenvalue system in the form

$$\lambda\tilde{\boldsymbol{b}} = -\boldsymbol{u}\cdot\nabla\tilde{\boldsymbol{b}} + \tilde{\boldsymbol{b}}\cdot\nabla\boldsymbol{u} + \varepsilon\nabla^2\tilde{\boldsymbol{b}} \equiv A\tilde{\boldsymbol{b}}, \tag{4.27}$$

where we have replaced $\boldsymbol{b}$ using (3.1) in (2.2). If our truncation is at mode number N, then we have $M = O(N^3)$ modes in $\tilde{\boldsymbol{b}}$ and so A is an $M \times M$ matrix with approximately $7M$ non-zero entries, since each mode couples to itself via diffusion and to 6 neighbours from the flow $\boldsymbol{u}$. Thus A is very sparse and would be impractical to store it explicitly for large N, even using a sparse matrix format. However the ARPACK software never requires the storage of A, only that one can evaluate it on a vector $\boldsymbol{w}$. In fact, while it is not the case for this application, A could even be a large full matrix which simply arises from a linear transformation on the vector: provided this linear transformation can be calculated, the eigenvalue solver may be used.

We implemented the Arnoldi solver for the dynamo problem as follows. Given a vector $\boldsymbol{w}$ with M complex entries,

- A routine 'unpacks' $\boldsymbol{w}$ by placing successive elements of the vector as magnetic field mode components $\tilde{\boldsymbol{b}}_{l,m,n}$ for modes in the fundamental domain $\mathcal{G}_N$ (4.9). For representations III, IV and V the various fields $(\tilde{\boldsymbol{b}}_j)_{l,m,n}$ are unpacked in turn. We omit the details, which are straightforward and follow the discussion of degrees of freedom outlined in Appendix B.
- Modes that neighbour $\mathcal{G}_N$ are filled in as detailed in section 4.2 according to the representation in use. This employs the same routines as in the time stepping codes.
- $A\boldsymbol{b}$, the right-hand side of (4.27), is now evaluated. Note that this is almost the same as time stepping the time evolution problem (2.2) and only the diffusion terms are treated differently, otherwise the routine used is from the time stepping code. The results for the magnetic field $\tilde{\boldsymbol{b}}$ for I and II, or fields $\tilde{\boldsymbol{b}}_j$ for III, IV and V are stored.
- These fields are now 'packed', mode by mode, back into a vector $\boldsymbol{w}$, precisely the inverse of the first step, and this is returned to the ARPACK routine.

One important difference between this eigenvalue solver method and time stepping the original PDE, is that Hermitian symmetry can no longer be exploited to reduce the number of modes and so the computational time: it is necessary to work with all the modes in $\mathcal{G}_N$. One could write down a map from modes in $\mathcal{H}_N$ to $\mathcal{H}_N$ that corresponds to evaluating the right-hand

side of (4.27), and this would easily be available from the time stepping codes, but such a map involves complex conjugation and would destroy the linearity of the operation $\boldsymbol{w} \to A\boldsymbol{w}$ required for any eigenvalue solver.

A second important difference concerns the degrees of freedom of the magnetic field in Fourier space. Focusing on $\mathcal{G}_N$ for the sake of argument, the symmetries for a given representation may require certain modes on the boundary of $\mathcal{G}_N$ to be zero, or to be related to other modes. For the purposes of time stepping this is not important, and these conditions are not imposed explicitly on the field in our simulations. (In addition some of these component fields are forced to be real from Hermitian symmetry, but this is not relevant to the Arnoldi solver.) Initially these conditions were not imposed on magnetic fields for the Arnoldi solver, but it was found that often this converged to a spurious solution (in which the conditions do not hold) and spurious eigenvalue or, more often, was unable to converge to one at all.

Thus the vector $\boldsymbol{w}$ that holds all the magnetic field information is required to contain precisely the correct number of degrees of freedom, without duplication or zeros. To do this we start by exploiting $\nabla \cdot \tilde{\boldsymbol{b}} = 0$ to reduce the number of components per mode to two instead of three. Given that $l \neq 0$ in $\mathcal{G}_N$ we may always reconstruct

$$\tilde{X}_{l,m,n} = -l^{-1}(m\tilde{Y}_{l,m,n} + n\tilde{Z}_{l,m,n}) \tag{4.28}$$

and so only store $\tilde{Y}_{l,m,n}$ and $\tilde{Z}_{l,m,n}$. The next step is to consider modes on the boundary of $\mathcal{G}_N$ which are mapped to themselves or to other boundary modes under symmetries, leading to either duplicated information, or modes forced to be zero. After these considerations, $\boldsymbol{w}$ may be taken to contain only the minimal set of modes, and the unpacking routine recreates everything from these; the details are in Appendix B.

R_m	rep	N	dt	T	memory	comp time
10	I	8	0.01	200	1196KB	1s
	II	8	0.01	200	1196KB	1s
	III	8	0.01	200	1460KB	1.5s
	IV	8	0.01	200	1720KB	2s
	V	8	0.01	200	1720KB	2s
100	I	22	0.005	800	4892KB	2m 44s
	II	22	0.005	200	3836KB	41s
	III	22	0.005	800	7268KB	3m 47s
	IV	22	0.005	200	8588KB	1m 11s
	V	22	0.005	300	8852KB	1m 48s

Table 3
Typical values for time stepping codes

Two values R_m (one low, one intermediate) were chosen to demonstrate the major differences between time stepping (table 3) and the Arnoldi solver (table 4), these being $R_m = 10$ and 100. To facilitate the comparison between these very different methods, the only parameter common to both, the resolution, has been standardised as $N = 2R_m^{1/2}$. The resolution required scales as $R_m^{1/2}$ (Moffatt & Proctor, 1985; Galloway & Frisch, 1986) and these values for N

R_m	rep	N	# of solns	basis vectors	memory	comp time
10	I	8	1	7	1424KB	$\ll$ 1s
	II	8	1	7	1452KB	$\ll$ 1s
	III	8	1	11	1656KB	$\ll$ 1s
	IV	8	1	15	1872KB	$\ll$ 1s
	V	8	1	11	1860KB	$\ll$ 1s
100	I	22	2	110	14MB	2m 24s
	II	22	1	80	11MB	1m 34s
	III	22	5	184	44MB	11m 35s
	IV	22	4	250	86MB	17m 59s
	V	22	2	230	79MB	10m 30s

Table 4
Typical values for Arnoldi eigenvalue solver code

have been tested to provide safe resolutions for convergence of growth rates to three significant figures.

The space of parameters particular to each method has been explored so that the optimal values for solutions to have converged are known. In the case of the Arnoldi eigenvalue solver this is the minimum number of basis vectors, whereas for time stepping, these are the largest possible time step dt and shortest simulation time T. Values are given in the tables. The numbers of solutions found are noted in table 4 as it identifies one of the difficulties with the Arnoldi solver, namely that it does not always locate the eigenvalue with the largest real part unless it is set to compute multiple eigenvalues. This seems to occur when there are several eigenvalues whose real parts are of the same order of magnitude. For example, in representations II and III at $R_m = 100$, class II has one overridingly dominant eigenvalue whereas class III has several modes which are decaying at similar rates. This is an inherent weakness with the Arnoldi solver method as one has to vary not only the minimum number of the basis vectors but the number of eigenvalues to be computed, to ensure that the dominant one is actually found.

Additionally, for the ABC dynamo problem, the setting of parameters for convergence can be very sensitive to the value of R_m, as the minimum number of basis vectors required can increase by an order of magnitude with a small change in R_m. This sensitivity could, however, be indicative of more interesting structure within each representation that, through time stepping, we are unaware of. Figure 7 identifies such a case, where crossings occur in sub-dominant branches. In our experience, the only systematic means of finding the minimum number of basis vectors for convergence is by brute force, rerunning simulations for fixed R_m and incrementing the number of basis vectors until the routine succeeds in finding one or more eigenvalues (depending on the number desired). For low and intermediate R_m, this is not too problematic, as simulations are relatively fast (on the order of minutes), but since increasing the number of basis vectors will also increase the computer time for a given simulation, this becomes extremely difficult with $R_m = O(10^3)$. The fact that we are unable to determine in advance whether the routine will converge until it has ended, is at the core of the problem, although a similar problem arises with time stepping, as it can be difficult to determine whether the

field has settled to a final state or is in a long transient (an example being representation V at $R_m = 215$).

For lower and intermediate R_m, the Arnoldi method can be very informative, as it has the ability to find more than one eigenvalue branch (see figure 7). Currently, through time stepping, we can only calculate the real and imaginary parts of the dominant eigenvalue; however there are multiple branches of solutions, corresponding to different eigenvalues, which can provide insight into alternative (although less effective) dynamo mechanisms and the nature of branch crossings.

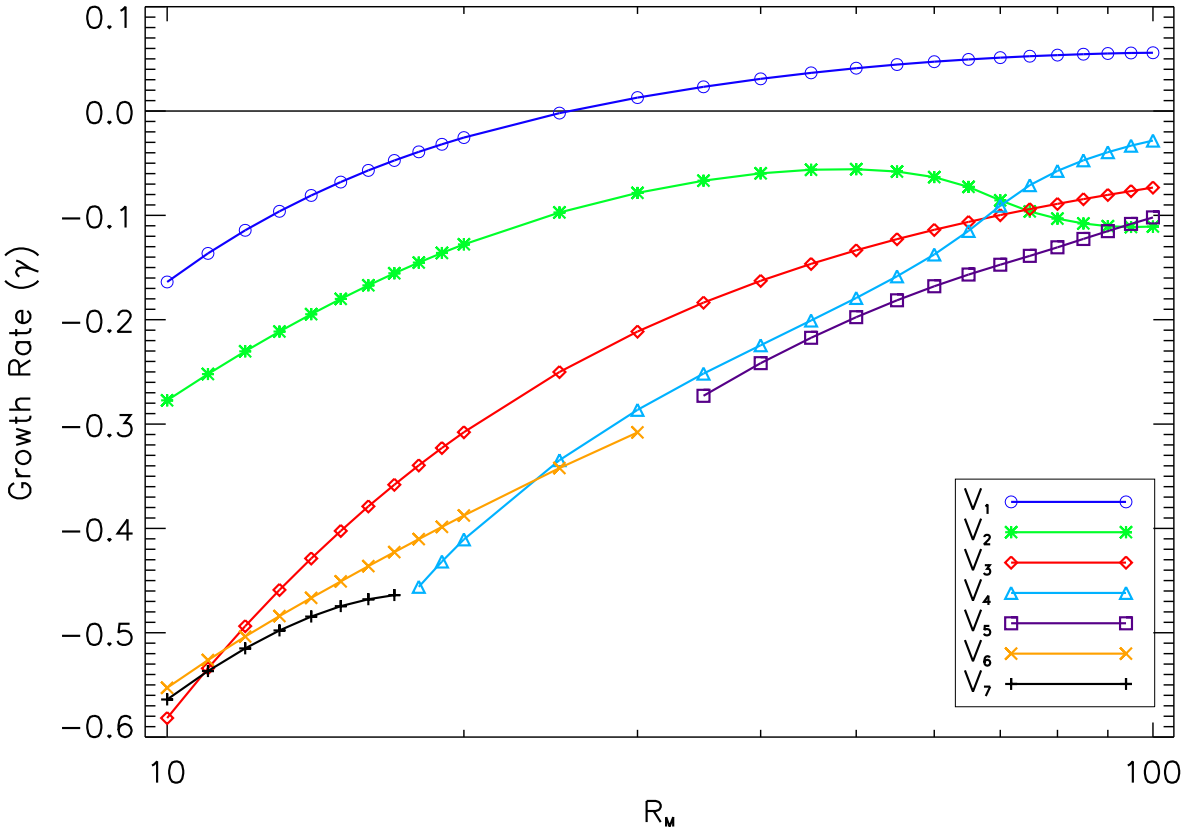

Fig. 7. Growth rates for seven branches of solutions for class V, $R_m = 10$ to $R_m = 100$.

Note that because of local mode interactions in spectral space, parallelisation of our spectral ABC time stepping codes can be achieved without much difficulty. We divide the full range of l into a set of (generally unequal) subranges, assigning each subrange to a computer core. After each time step, the memory assigned to each core is updated with the necessary magnetic field modes from contiguous cores. The boundary modes displayed in figure 5 are then updated before all modes are again stepped in time; we omit further details. Parallelisation was employed for $R_m \geq 3000$. In a comparison at $R_m = 1000$, time steps took on average 9.0×10^{-2}s on a desktop machine using a single core, whereas time steps took on average 8.6×10^{-3}s using a single node (12 cores in parallel), showing a speed up of around ten times.

5 Growth rates and magnetic field structure

In this section we give the results of our simulations.

5.1 Growth rates & frequencies

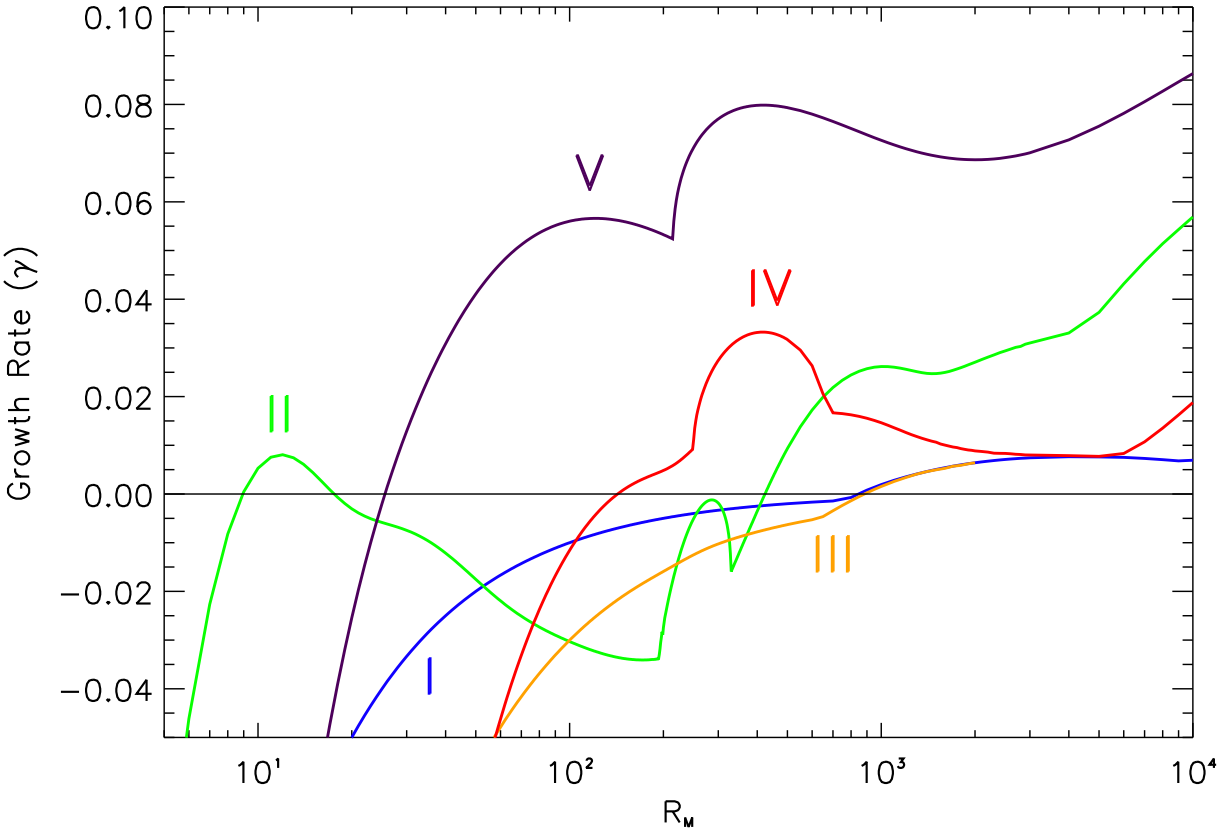

Fig. 8. Growth rates of the representations of ABC dynamos for R_m up to 10^4

The growth rates for magnetic fields in all of our simulations are summarised in figure 8, showing growth rate $\gamma = \mathrm{Re}\,\lambda$ versus R_m. For the 1:1:1 ABC flow, fields in only two of the symmetry classes provide the dominant dynamo mechanism, namely those of classes II and V. As discussed in Galloway & Frisch (1986), there are two distinct windows of dynamo action, separated by a brief interval of purely decaying fields over the range of $R_m \approx 17.5$ to $R_m \approx 27$. The fields in the second window were referred to as 'symmetry-breaking', as they have fewer apparent symmetries than fields in the first window. It is now clear that fields in the second window belong to symmetry class V, and this remains dominant in our simulations up to $R_m = 10^4$, and up to 2.5×10^4 in Bouya & Dormy (2013) (where the growth rate begins to level at approximately 0.1). The branches II, IV and V give growth rates that show no sign of tending to zero in the large R_m limit, suggestive of fast dynamo action. However the limiting values for large R_m cannot be assessed from the present results. Interestingly, it can be seen from figure 9 below that boosts in growth rates for classes II and IV at high R_m are linked to mode changes within the classes.

Symmetry classes I and III have also been established to contain dynamos, but show the lowest growth rates and last onset as R_m is increased. In both cases, difficulties were encountered with calculating the leading growth rate, as fields in these two classes show long, slowly evolving transients, particularly in class III. Limitations of computer time have not allowed us to explore values of R_m for class III beyond those shown in figure 8. In class I, until the mode change at $R_m \approx 800$, the field with the largest growth rate is the trivial solution, with $\boldsymbol{b} = \boldsymbol{u}$, $\gamma = -R_m^{-1}$. It is important to note that without enforcing symmetries, the dynamo growth rate will simply be the envelope of the individual growth rates of the symmetry classes, meaning that the growth rate of only the fastest growing dynamo for a given R_m will be calculated.

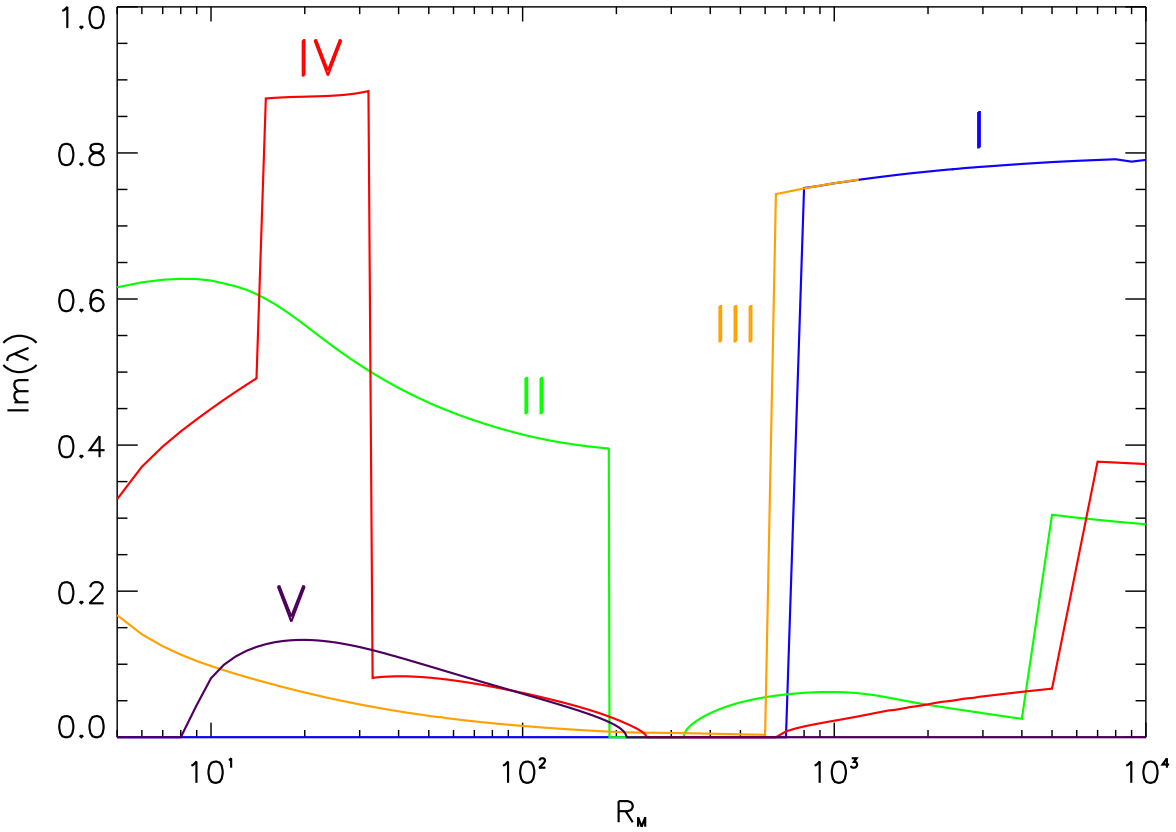

Fig. 9. Frequencies for the ABC dynamos plotted against R_m.

The imaginary parts of the eigenvalues, corresponding to (half of) the frequencies of the magnetic energy oscillations, are shown in figure 9. Since the eigenvalues occur in complex conjugate pairs, the absolute value of the imaginary part is plotted. It is apparent that some of the modes, within each symmetry class, are steady (real eigenvalue), whereas others are oscillatory (complex eigenvalue). Transitions between steady and oscillatory modes for a given symmetry class may occur because of a mode crossing (giving a discontinuity in the frequency) or because of eigenvalue coalescence (in which the frequency tends to zero with a square root dependence). This is discussed recently in Bouya & Dormy (2013); our results agree with theirs for the fastest growing mode at each R_m (as symmetry is not imposed) and we refer to this paper for further discussion including a phase plane analysis. Here we simply note that the kink in the dominant representation V curve around $R_m \simeq 215$ was a source of difficulty for Galloway & Frisch (1986) as very slow oscillations led to uncertainty in the growth rate. It was not possible at the

time to determine whether this corresponds to a real eigenvalue or two complex eigenvalues with small imaginary parts. It is now clear that the frequency goes to zero below this point, where two complex eigenvalues coalesce to give a leading real eigenvalue above it (Bouya & Dormy, 2013); naturally there is also a subdominant real eigenvalue.

In addition to this there are changes in the eigenvalues for other, subdominant symmetry branches. For branch II there is a mode crossing (within representation II) at around $R_m \simeq 190$ giving a discontinuous jump from a non-zero frequency to a real eigenvalue followed by eigenvalue de-coalescence as R_m increases above 329 and the branch becomes oscillatory. Likewise for branch IV there are mode changes followed by eigenvalue coalescence and de-coalescence (at $R_m \simeq 249$ and 675 approximately). In class III, the frequency appears to be decreasing rapidly as R_m increases, prior to the mode change at around 620. For larger R_m, an increase in frequency is seen, closely matching the frequency profile for class I, which may be related to the similarity in the structure of their magnetic fields as discussed below

5.2 Field structures

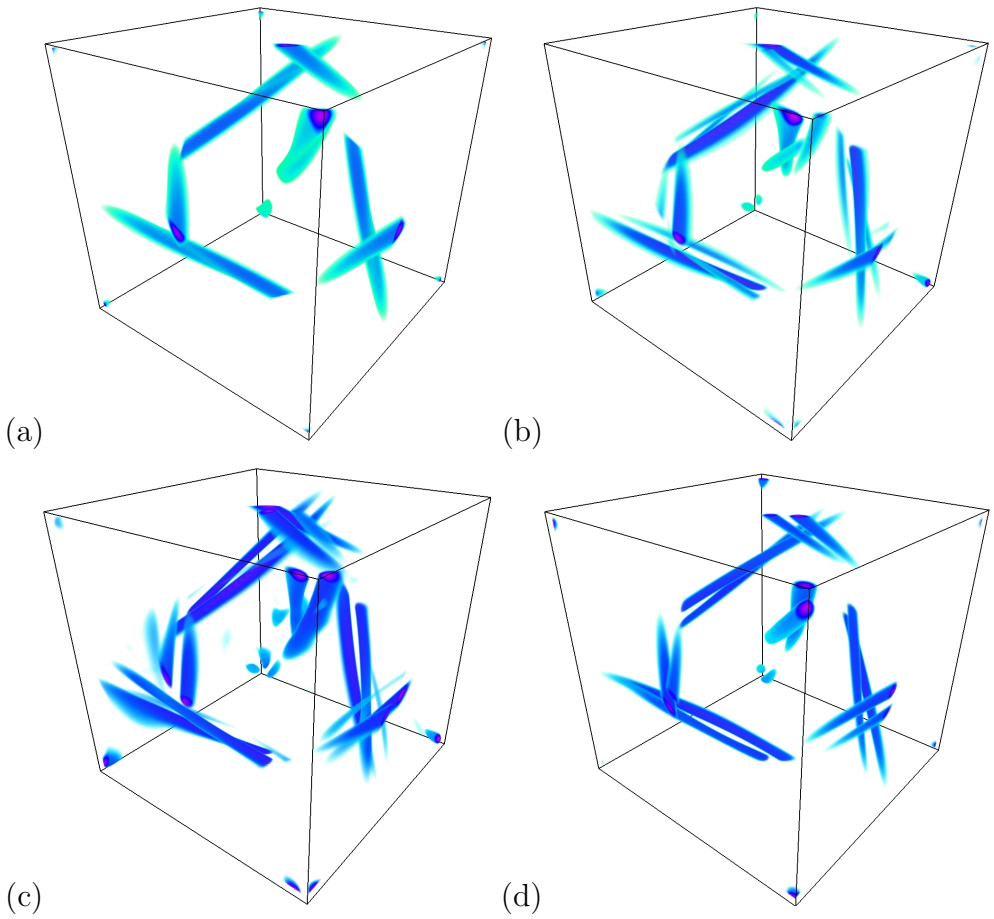

Fig. 10. Visualisations of magnetic field strength $|\boldsymbol{B}|$ for (a) II to d) V for $R_m = 100$

Figure 6 gives examples of plots of total magnetic energy versus time for two oscillatory cases (a,b) and one steady case (c). In the oscillatory cases, the structure of the field is time dependent and we have visualised fields over times during a cycle. The symmetries in each class force the magnetic field to take certain arrangements, leading to the individual structures that are seen

in figure 10, which shows snapshots of the strongest fields in three dimensions for $R_m = 100$. We see the familiar cigar-like structures (which we simply refer to as 'cigars' in what follows), some single and some multiple, concentrated on the straight-line heteroclinic connections, or separatrices, determined by Dombre *et al.* (1986). Note that we have chosen a moderate value of R_m as visualisations at larger values simply give similar, but more concentrated structures and are in practice harder to interpret. We do not show the field for class I, at this value of R_m, which is just $\boldsymbol{b} = \boldsymbol{u}$.

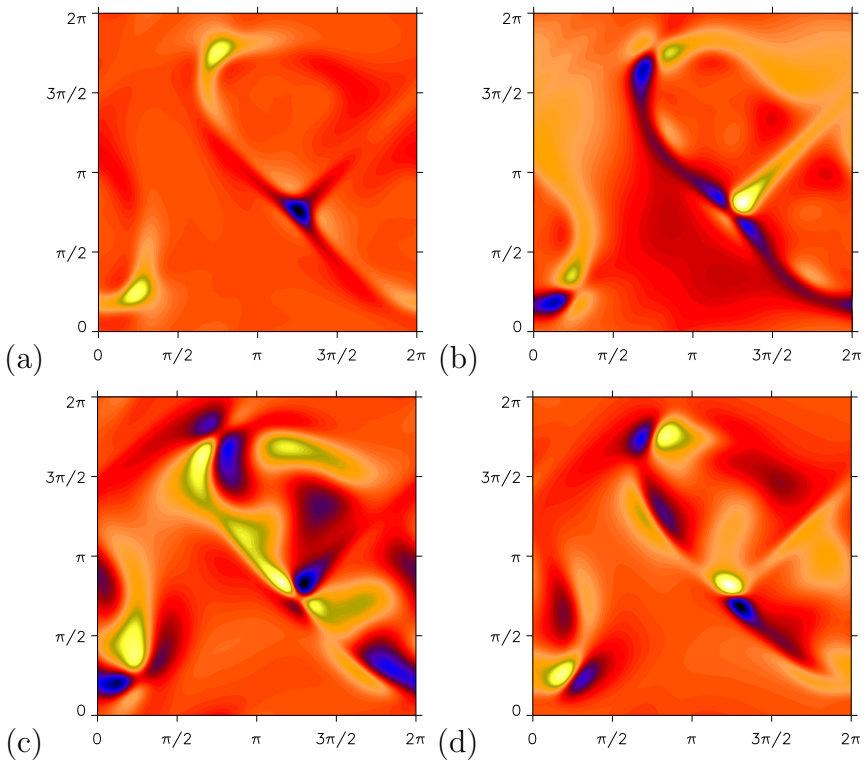

Fig. 11. Visualisations of magnetic field component b_z on a cross section $z = \pi/4$ for (a) II to (d) V with $R_m = 100$.

The remaining classes II to V are all oscillatory at this value of R_m and have similarities in structure but differences in detail. To give another view we show in figure 11 the field component b_z perpendicular to a slice $z = \pi/4$ through the fluid domain. For reference figure 12 (after Dombre *et al.*, 1986) shows Poincaré sections for $z = 0, \pi/4, \ldots$ reading across then down. There is a network of thin bands of chaos visible, and in between (the white regions), there is integrable motion, referred to as the 'principal vortices' of the flow. The second of the sections, $z = \pi/4$ is relevant to figure 11. At this value of z there are stagnation points $\boldsymbol{u} = 0$ lying at $\boldsymbol{r}_1 = (5, 3, 1)\pi/4$ (with a 2-d stable manifold, 1-d unstable manifold, type 'α') and $\boldsymbol{r}_2 = (7, 5, 1)\pi/4$ (with a 2-d unstable manifold, 1-d stable manifold, type 'β'). There are also two points lying on the straight-line separatrices that join stagnation points namely $\boldsymbol{r}_3 = (1, 1, 1)\pi/4$ and $\boldsymbol{r}_4 = (3, 7, 1)\pi/4$.

In each symmetry class from II to V in figure 10 the field has concentrations along the separatrices joining stagnation points, and this is evident in the panels in figure 11, where the values of b_z are large near to $\boldsymbol{r}_1$, $\boldsymbol{r}_3$ and $\boldsymbol{r}_4$. At the stagnation point $\boldsymbol{r}_1$ the 2-d stable and 1-d stable manifold act to concentrate magnetic fields into flux ropes and these are then visible along separatrices, e.g. at $\boldsymbol{r}_3$ and $\boldsymbol{r}_4$. In each case, the field is not significant at $\boldsymbol{r}_2$, unsurprisingly

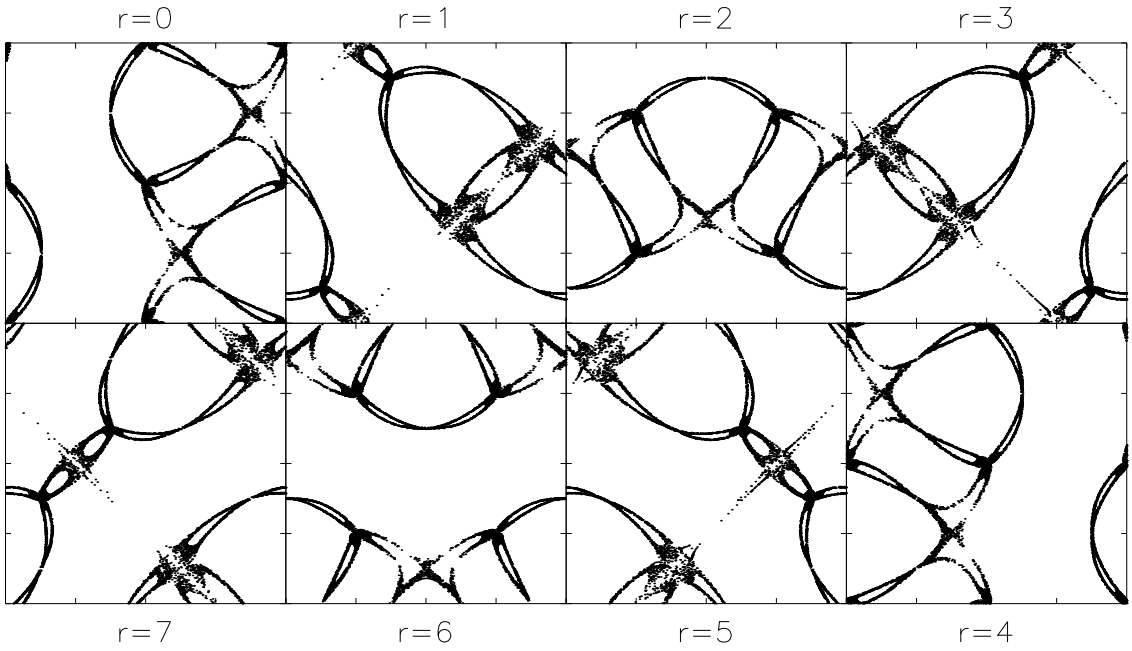

Fig. 12. Poincaré sections of particle trajectories in the 1:1:1 ABC flow, crossing the planes of $z = r\pi/4$ for $r = 0, 1, ..., 7$, reading across then down.

since here the 2-d unstable manifold acts to repel field. As all the modes are oscillatory for this value of R_m, the fields in the cigars change sign during a single cycle. However the structures and the way this occurs differs in the different representations and we now remark on this (based also on other visualisations not shown here).

In classes IV and V, the field is twisted around (but never lies on) the separatrices with the dominant fields consisting of four and two flux tubes respectively. In the oscillating branch for class V, the pair consists of a minor (weak) and a major (strong) flux tube, each with different polarity, eventually reversing polarity and switching roles. Class IV contains two pairs, each pair consisting of a positively and a negatively directed flux tube but with one pair being dominant (strong) and the other subdominant (weak). As in class V, these pairs feed off one another until a critical point is reach (lowest total energy in the cycle) and the fields reverse polarity and switch roles.

Before the emergence of the growing mode in class I, the slowest decaying mode is simply the trivial solution $\boldsymbol{b} = \boldsymbol{u}$. In the growing mode that emerges at $R_m \sim 800$ we see something much more interesting: the magnetic field is formed as 'flux ropes', centred around the six principal vortices. Each flux rope consists of six individual flux tubes, each tube with varying strength along its (periodic) length. This structure can be clearly seen in figure 13 (a,b) and the cross section of b_z at $z = \pi/4$ reveals the alternating polarity of these tubes. The flux ropes in classes I and III (below) closely resemble the structure of fields in smooth Ponomarenko dynamos (Ponomarenko, 1973). This is well known as a slow dynamo mechanism, relying on diffusion in curved geometry and shear to give a dynamo cycle (Gilbert, 1988; Ruzmaikin, Sokoloff & Shukurov, 1988). Our current results indeed show falling growth rates for these branches as $R_m \to \infty$, in keeping with this interpretation.

Class III is intriguing in that it has features that resemble both the structures of class I and those of classes II, IV and V. Before the emergence of the growing mode, the field switches between two states. In its first state, the field is concentrated along four of the six principal

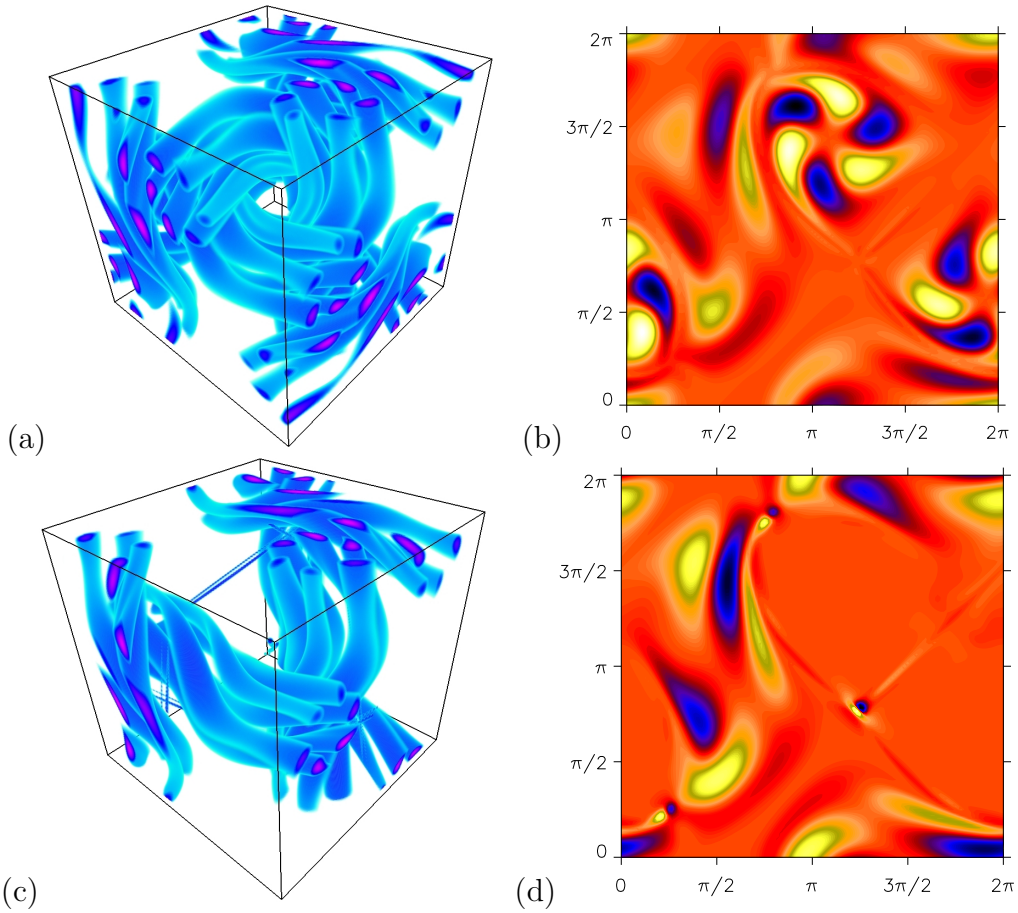

Fig. 13. Magnetic field strength ($|\boldsymbol{B}|$) for (a) class I and (c) class III and field component b_z at $z = \pi/4$ for (b) class I and (d) class III, for $R_m = 1000$.

vortices of the flow and in the second state, the field forms three flux tubes, containing a major and two minor flux tubes (with the opposite polarity to the major), and all twisted around the separatrices. Over a single cycle, the magnetic field jumps between these two states, each time reversing polarity so that each state occurs twice in one cycle. Figure 11 (b) shows class III in the second state described. In the growing mode, however, which emerges at $R_m \approx 650$, we have a combination of the two states, with the flux ropes, seen in class I, concentrated around four of the six principal vortices and only two apparent flux tubes (of opposite polarities) twisted around the separatrices. This structure can be seen in figure 13 (c,d). Note that the fact that we see field in four of the six principal vortices seems surprising — why these four? — but is ultimately a result of our choice of matrices employed for III; with this our visualisations (for III, IV, V) have an element of arbitrariness although the eigenvalues do not.

For class V, a full cycle of field evolution is displayed in figure 14 at eight different times for $R_m = 100$. The snapshots were taken so that the evolution of the field could be seen as clearly as possible, though some explanation is required. The start of the cycle was fixed as the time at which the energy is at its minimum and the snapshots were normalised to account for the growing field. At the start of the cycle, we see lone flux tubes at the stagnation point $\boldsymbol{r}_2$ and at the midpoints $\boldsymbol{r}_3$ and $\boldsymbol{r}_4$. These flux tubes weaken as secondary flux tubes of opposing polarity develop alongside them until by $0.45T$, the secondary flux tubes are stronger. Between $0.45T$ and $0.46T$ (frames 3 and 4), a reversals occurs so that when the secondary flux tube reaches full strength and the primary tube is diminished, the field has returned to a state similar in

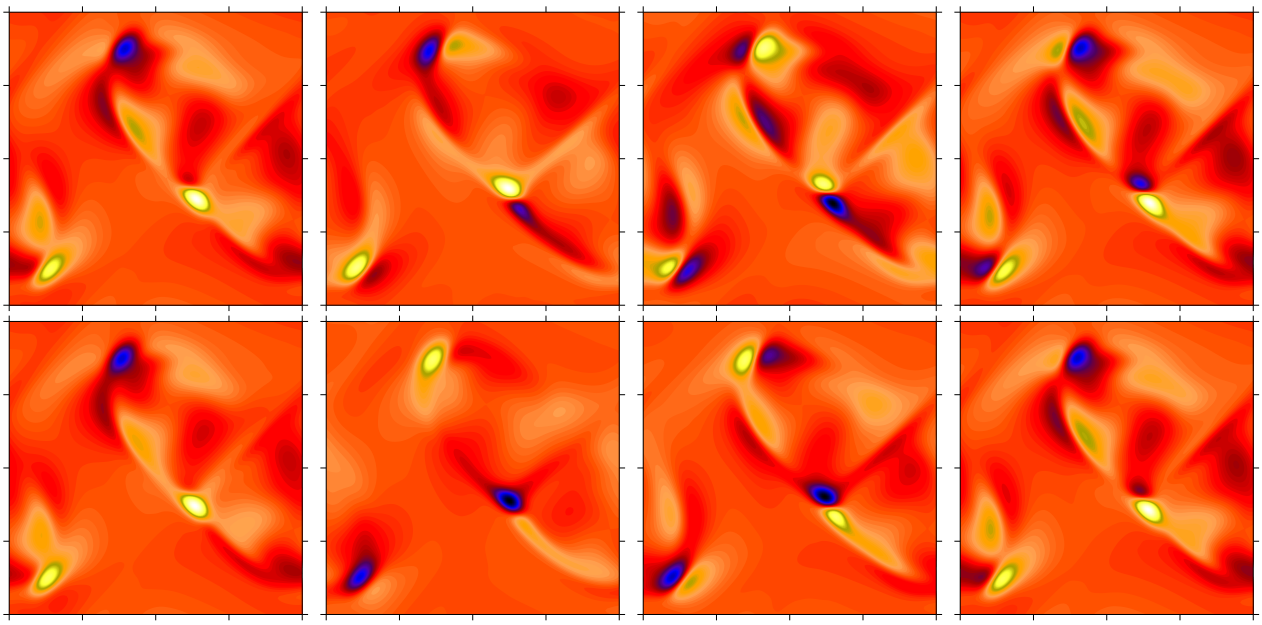

Fig. 14. Magnetic field component B_z at $z = \pi/4$ for times $t = 0$, $0.2T$, $0.45T$, $0.46T$, $0.52T$, $0.57T$, $0.8T$ and $0.99T$ for class V, $R_m = 100$. Blue (dark) represents negative field strength and yellow (light) represents positive.

appearance to its original configuration at $0.52T$. Between $0.52T$ and $0.57T$, multiple field reversals occur, each on a timescale of order $0.01T$ or less, until by $0.57T$ the configuration settles as the reverse of that at $0.52T$. Again, a secondary flux tube emerges and grows while the primary diminishes so that by $0.99T$, the configuration has almost returned to that of the start. This process describes the dominant dynamo mechanism for $R_m > 24$, with the period of this cyclic behaviour increasing until at $R_m \approx 215$, the period becomes infinite and the structure of the dynamo is no longer time dependent, though the field amplification process remains the same (see Dorch, 2000). The final field configuration can be seen in figure 15 at $R_m = 250$. As R_m is increased, the structure of this dominant mode remains the same, although the flux tubes are confined to an ever smaller region, making it increasingly difficult to visualise at higher R_m.

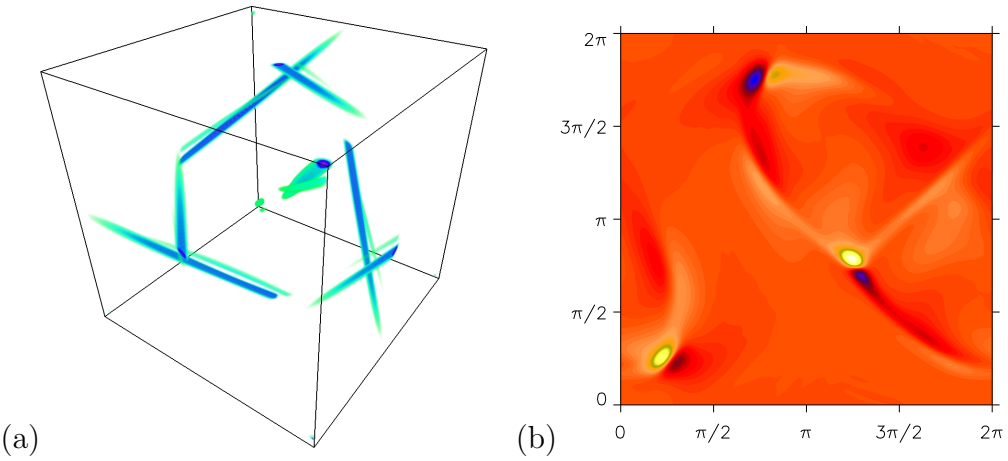

Fig. 15. Visualisations of (a) magnetic field strength ($|\boldsymbol{B}|$) and (b) field component b_z at $z = \pi/4$ for class V, $R_m = 250$.

Spectra of magnetic energy reveal some differences between the representations that mirror

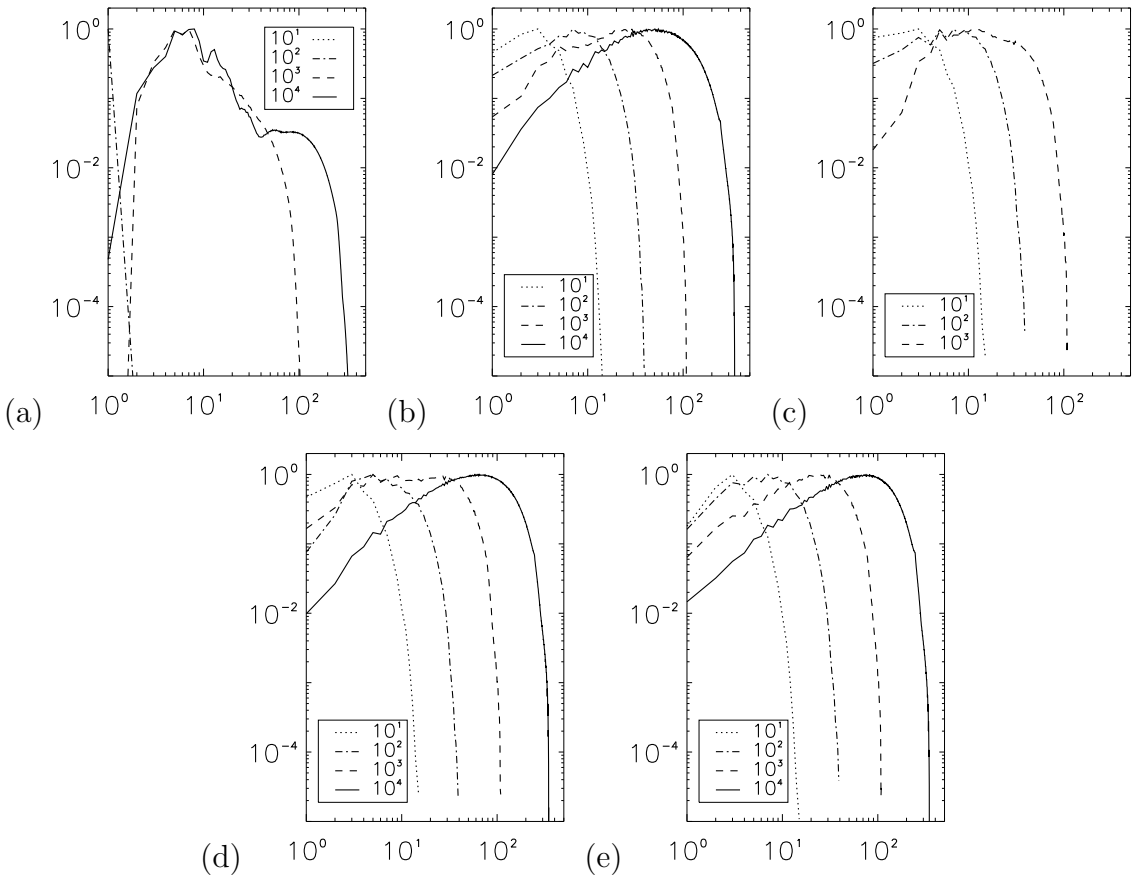

Fig. 16. Energy spectra displaying normalised magnetic energy against wavenumber k (log-log) for (a) I to (e) V, at $R_m = 10^1, 10^2, 10^3, 10^4$.

the structure of the fields in real space. In figure 16, it is seen that for representations II, IV and V a spectrum with a power law dependence of approximately k emerges at large R_m: this is consistent with the concentration of magnetic field in isolated flux tubes. (In fluid dynamics similar tubes of vorticity would correspond to an energy spectrum of k^{-1} and so a vorticity spectrum of k.) However for representation I there is considerable energy at large scales consistent with the broader spatial scales of a slow dynamo maintained by weak stretching in the principal vortices, while III shows a rather flatter spectrum whose relationship with the complicated physical space picture is unclear.

6 Growth rates and structure for fluid stability of ABC flows.

In this section we consider the fluid stability problem given in (2.4) for a perturbation $\boldsymbol{v}$ to the ABC Navier–Stokes flow $\boldsymbol{u}$ (2.1), maintained against viscosity by a body force. The same symmetry considerations apply as for the dynamo problem, but the results are very different. Figure 17 shows growth rates and figure 18 frequencies for each branch as a function of R_e, obtained numerically using codes for which symmetry is built in, and checked against a code with no assumption of symmetry.

To test our results, we referred to Galloway & Frisch (1987), who numerically solve this problem up to $R_e \approx 200$. We obtain the same branch of solutions for the range of R_e that they studied and identify it as class V. In parallel with the magnetic case, all five symmetry classes contain

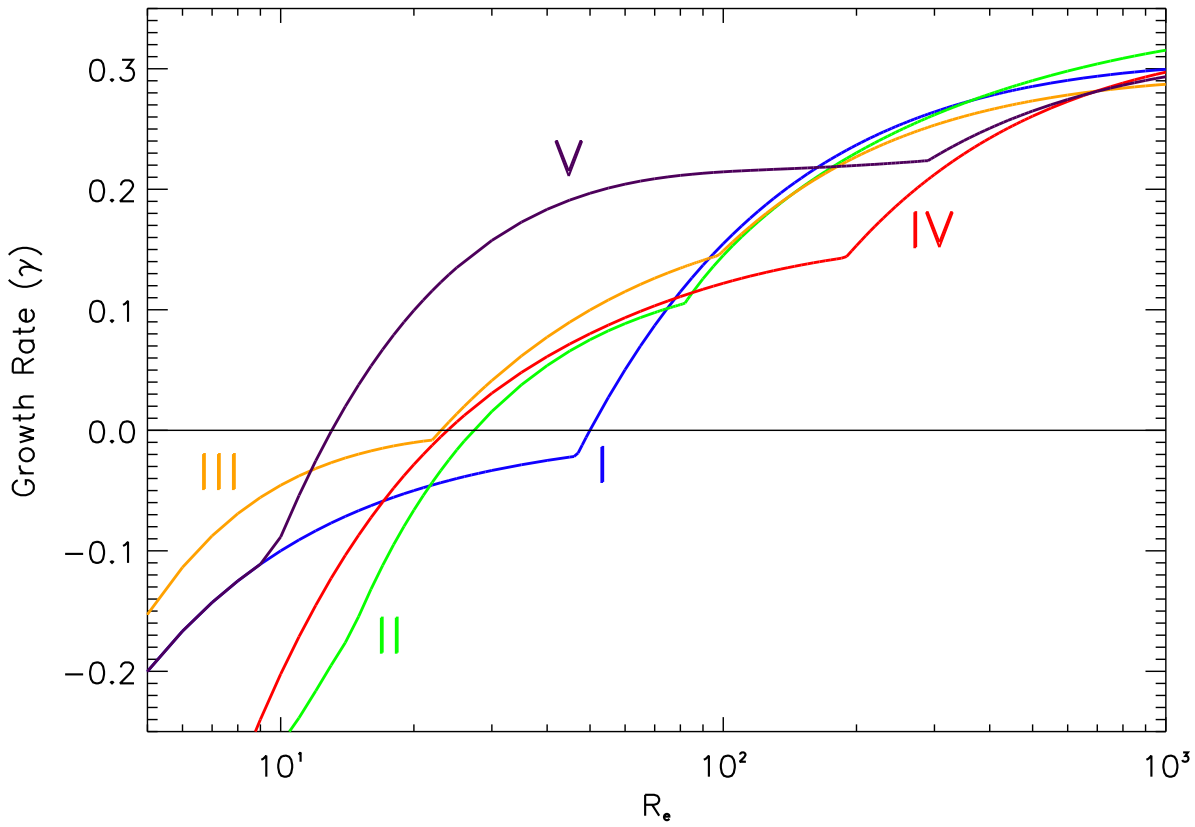

Fig. 17. Growth rates for fluid instability in the ABC flow.

flows in which the growth rate of the instability is positive. The first flow to become unstable is in class V and this occurs somewhere in the interval $R_e \in [13, 14]$. As R_e is increased, classes III, IV and II follow, with class I the last to have an unstable mode, emerging at $R_e \approx 50$. Class V remains the most unstable flow until $R_e \approx 160$, at which point a flow in class I becomes the dominant mode. It is then superseded by a steady mode in class II at $R_e \approx 370$, with this mode remaining dominant up to the largest R_e simulated. In contrast to the magnetic problem, all classes have remarkably similar growth rates at large R_e.

Note that the dominant mode at $R_e = 10^3$ in class II, is steady, as with the dominant mode in the magnetic problem. Class II is the only one in which the dominant modes have successively lower frequencies as R_e is increased and, of course, is the only class to contain a steadily growing perturbation as the dominant mode for intermediate and high R_e. The modes of classes I, III, IV and V at $R_e = 10^3$ are oscillatory with surprisingly little difference in their frequencies. Notably, classes I and III are very close in frequency, as are classes IV and V. We see no cases of eigenvalue coalescence or de-coalescence. We observe only discontinuous changes in frequency indicative of completely different modes emerging within each class.

The results that we have obtained indicate that the symmetries play a less crucial role in the fluid instability problem. Figures 19 and 20 are visualisations of the flow structures in each class at $R_e = 300$. This value was chosen, as by this point, the dominant modes are on the same branches as the dominant modes at $R_e = 10^3$, and so the flows have a similar structure but are not so concentrated around the separatrices. In each case the strongest velocity fields are linked to separatrices, but the second of these figures shows much more overall structure in a cross section, than in the magnetic case.

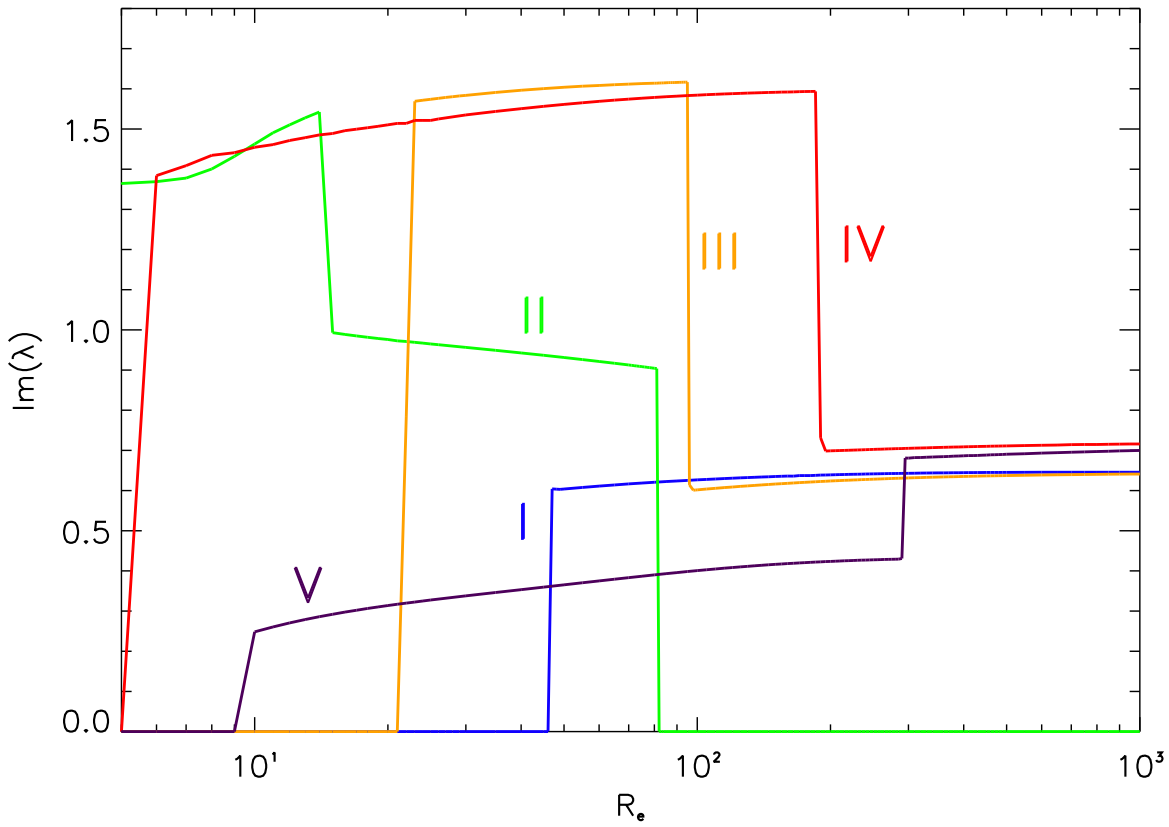

Fig. 18. Frequencies for fluid instability in the ABC flow.

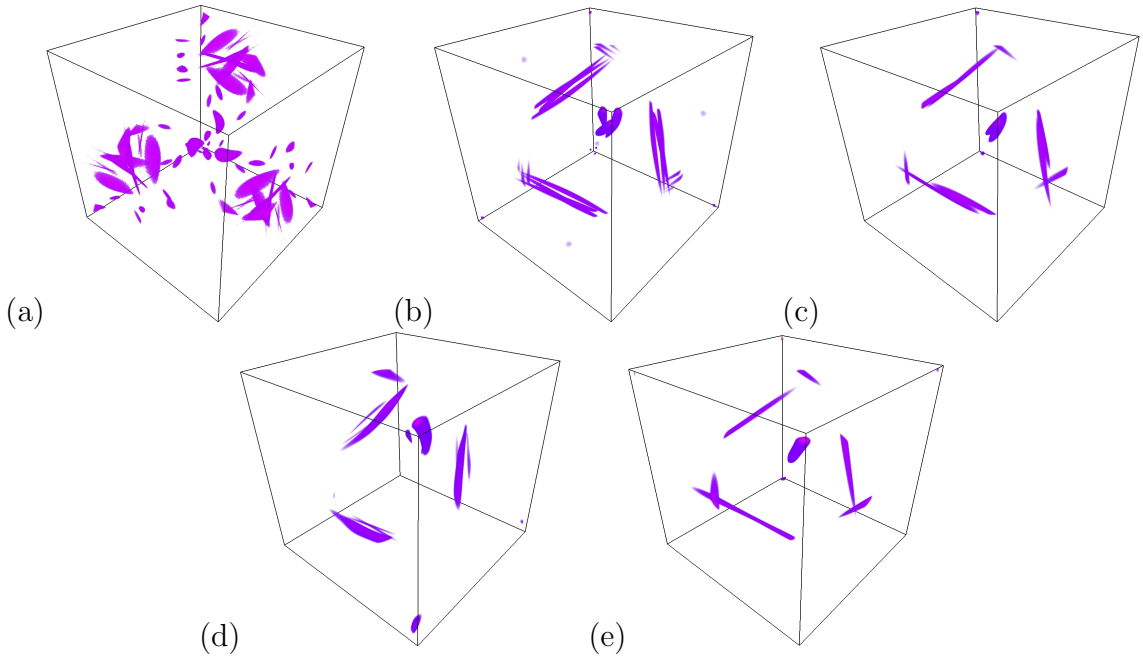

Fig. 19. Visualisations of magnitude of fluid instability $|\boldsymbol{v}|$ for (a) I to (e) V for $R_e = 300$

The dominant flows in classes II–V are reminiscent to those of classes II, IV and V of the magnetic problem. There is no analogue of the magnetic field concentration in principal vortices observed for representations I and III. We see that imposing the symmetries forces the flows

into certain configurations. Class II includes three tubes of strong flow concentrated around the α-type stagnation point that are stretched equally towards the β-type stagnation point. Referring to the cross section of v_z at $z = \pi/4$, the flow in two of the tubes is of the same sign, or direction, with the third of the opposite sign. Note that in this class, strong flows also exist that surround the β-type stagnation points; these are not seen in figure 19(b) but are in figure 20(b). Class III has two tubes of flow centred on the α-type stagnation point. These two tubes are joined at the stagnation point, however, with each tube stretched towards a different β-type stagnation point. These connected tubes are of the same sign, seen as a flat area of strong flow at $\boldsymbol{r}_1 = (5, 3, 1)\pi/4$ in 20(c).

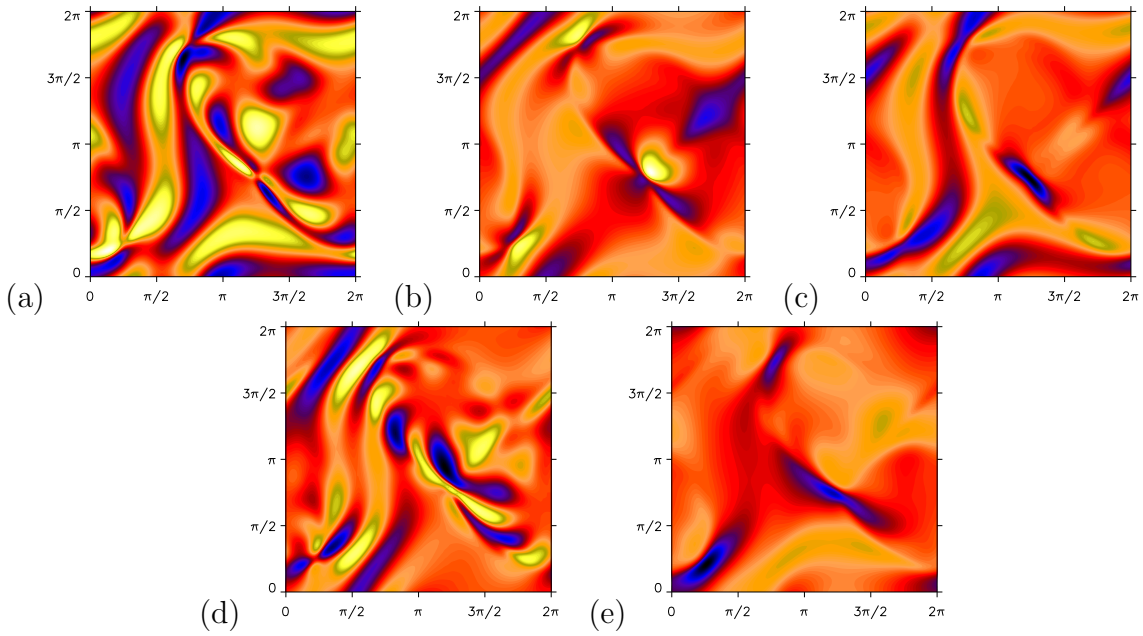

Fig. 20. Magnitude of fluid instability component v_z for (a) I to (e) V for $R_e = 300$ at $z = \pi/4$

The most unstable flow in class IV includes a single major and multiple minor tubes centred on the α-type stagnation point. The cross-section is less revealing than others, though we can identify stronger flows near $\boldsymbol{r}_2$ and relatively strong flows in the principal vortex that runs vertically on the left-hand side of the section. The strongest flows in class V are, again, centred on the α-type stagnation points and are stretched into the classic cigars, though appearing more flattened than their counterparts in the magnetic case. These features resemble those of figure 2 in Galloway & Frisch (1987), which appears to belong to the same branch of solutions as those in class V.

The magnitude of the perturbation flow is difficult to visualise in class I, as there are many small features. The dominant flow here is situated around the separatrices connecting the α- and β-type stagnation points, rather than centred on the α-type stagnation points. However, three small beads of strong flow are also built up on the planes in which the streamlines of the flow enter the α-type stagnation points. In figure 20(a), we see that areas of flow are also loosely arranged around the principal vortices, suggesting that these also play a part in generating and magnifying the fluid instabilities. Overall, in comparison with the magnetic problem, the structures appear to be less ordered and much more loosely linked to the thin bands of Lagrangian chaos, with substantial flows in the principal vortices.

7 Discussion

In this paper we have studied the behaviour of the ABC 1:1:1 dynamo at large R_m and by exploiting symmetries have both reduced the computational effort and obtained distinct branches of solutions. These show a variety of field structures, in particular fields dominated by between one and three cigar-like structures on the separatrices, and fields that lie in the principal vortices, showing generation by a Ponomarenko-type mechanism. The results show that the second window of Galloway & Frisch (1986) remains dominant up to $R_m = 10^4$ and this has now been extended by Bouya & Dormy (2013) in a related study, with growth rates of around $\gamma = 0.1$ at $R_m = 2.5 \times 10^4$. It is interesting to compare these results with the rate of line-stretching (equal to the topological entropy for this flow) measured as $h_{\rm line} \simeq 0.09$ and the rate of growth of flux as $\Gamma_S \simeq 0.055$ in Childress & Gilbert (1995). The growth rates known at the largest values of R_m exceed both Γ_S and the rigorous upper bound of $h_{\rm line}$ (Klapper & Young, 1995). Either the latter has not been measured sufficiently precisely, or the growth rate γ has yet to reach a true large-R_m limit for the magnetic Reynolds numbers so far studied and must yet decrease. Certainly we do not see much evidence of the accumulation of sheets or tubes of flux in a chaotic region, but then this may be hidden as the line stretching rate $h_{\rm line}$ is distinctly smaller than the stretching given by the eigenvalue $\sqrt{2}$ at any α-type stagnation point. In other words it is difficult to separate the global chaotic stretching and folding from the strong local amplification at these stagnation points, and this is a topic for future analysis.

Certainly the growth rates and frequencies of all the branches do not seem to have really settled down for R_m up to 10^4 in our runs. We also note that idealised models of dynamo action in steady flows suggest the possibility of an infinite sequence of mode crossings with a growth rate that nonetheless converges to a limit; however with these crossings could be fields with increasing levels of structure along field lines and so the frequencies of the dominant modes would increase with R_m, while the growth rates would converge (Finn *et al.*, 1991; Childress & Gilbert, 1995). Indeed there are hints of the magnetic fields developing structure along field lines in the multiple field reversals noted for class V (see the discussion of figure 14).

Other elements of our study included testing the use of a sparse Arnoldi eigenvalue solver on this problem: this we found problematic at large R_m and here it appears that time stepping remains the best method available. Nonetheless at moderate R_m it is efficient and also allows one to find subdominant branches. We also investigated the fluid stability problem and followed branches in all five symmetry classes. Here it is striking that, unlike in the magnetic problem, the growth rates of all symmetry classes become similar at the largest Reynolds numbers studied, of around 1000. This strongly suggests instability mechanisms that are not closely linked to the behaviour of the base flow along the separatrices and so not closely constrained by the symmetries of the field. In contrast, in the magnetic problem, the stretching of field along these separatrices is a crucial part of the dynamo mechanism and so if a representation limits the types of field that can occur there, it has a strong impact on the growth rate. For the fluid instability the modes indeed are more dispersed than in the dynamo problem, although again the strongest flows are along the separatrices.

Future planned studies are to combine the codes here with those in Bouya & Dormy (2013) in order to push R_m to even larger values, and to investigate the alpha effect and large-scale dynamo fields, using a Bloch wavenumber formulation to allow fields of arbitrary scale. This is easily incorporated into the current code and again symmetries may be used to reduce the computational effort, one aim being to reproduce and extend results of Galanti *et al.* (1992).

We note that the 1:1:1 ABC flow was chosen for its high level of symmetry and well-established dynamo but it is known that other ABC flows have more substantial regions of chaos and faster growth rates, for example flows with $A = B \neq C$ (see Galloway & Frisch, 1986; Alexakis, 2011). Naturally these flows are less symmetric, with only eight of the 24 symmetries retained, in the case of $A = B$ those that map z to $\pm z$, namely $\mathsf{i}, \mathsf{a}, \mathsf{a}^2, \mathsf{a}^3, \mathsf{b}^2, \mathsf{c}^2, \mathsf{k}$ and n. This group is isomorphic to D_8 as discussed in section 3.1; following every representation gives only a 25% saving of computer time over a full simulation, although there is the advantage of obtaining all the branches independently. For A, B and C all unequal, only the symmetries $\mathsf{i}, \mathsf{a}^2, \mathsf{b}^2$ and c^2 are retained, this group being isomorphic to $\mathbb{Z}_2 \times \mathbb{Z}_2$, and there is no saving.

Finally we consider how the symmetry classes I to V impact on the presence or otherwise of cigars in the magnetic field problem. We consider the separatrix whose centre is at the α type stagnation point at $\boldsymbol{r} = -(1,1,1)\pi/4$ and introduce local cylindrical polar coordinates (ρ, θ, ζ) there (Gilbert, Ponty & Zheligovsky, 2011), given by

$$\begin{pmatrix} x \\ y \\ z \end{pmatrix} = -\begin{pmatrix} \pi/4 \\ \pi/4 \\ \pi/4 \end{pmatrix} + \begin{pmatrix} 1/\sqrt{2} & 1/\sqrt{6} & 1/\sqrt{3} \\ -1/\sqrt{2} & 1/\sqrt{6} & 1/\sqrt{3} \\ 0 & -2\sqrt{6} & 1/\sqrt{3} \end{pmatrix} \begin{pmatrix} \rho\cos\theta \\ \rho\sin\theta \\ \zeta \end{pmatrix}. \tag{7.1}$$

With this it may be checked that the action of d is to take $(\rho, \theta, \zeta) \to (\rho, \theta + 2\pi/3, \zeta)$ and the action of n is to take $(\rho, \theta, \zeta) \to (\rho, -\theta, -\zeta)$. We may consider potential cigar structures of the general form

$$\boldsymbol{b}_{\mathrm{c},m,n} = \hat{\boldsymbol{\zeta}}\rho^m \cos m\theta, \quad \boldsymbol{b}_{\mathrm{s},m,n} = \hat{\boldsymbol{\zeta}}\rho^m \sin m\theta, \tag{7.2}$$

It can be checked that under the action of d we have to restrict $m = 0 \bmod 3$ for I and II, while $m \neq 0 \bmod 3$ for III, and values of m are unrestricted for IV and V. This eliminates the possibility of a single cigar, i.e. a local, approximately axisymmetric ($m = 0$), ζ-independent structure, for representation III. If we look for a single cigar in representation I or II, then we observe that this is possible only in II (in which $M^{\mathrm{II}}(\mathsf{n}) = -1$), and similarly an $m = 0$ cigar is possible only in V and not in IV, of the three-dimensional representations.

This characterisation of the structures that can occur within a given symmetry classes has points of contact with figures showing magnetic fields in section 5.2 and the growth rates at the largest values of R_m in figure 8. We observe that the two modes showing the fastest growth rates are II and V, in which single cigars can exist. On the other hand I, III and IV show rather smaller growth rates to the right of this figure. Although these cases allow multiple cigars (that is $m \neq 0$) or more complex structures, the enhanced dissipation is likely to suppress growth rates at these R_m. Further study is planned of the cigars in real space and the link to symmetries.

Acknowledgements

We are grateful to Ismaël Bouya and Emmanuel Dormy for helpful comments and for sending us their paper in advance of its publication. We thank Mitchell Berger and Andrew Soward for useful discussions and the referees for constructive criticism. The larger calculations reported in this paper were performed using the University of Exeter Supercomputer. We are grateful to the authors of the package VAPOR, used for our three-dimensional visualisations; see Clyne

et al. (2007). Finally we are pleased to acknowledge the financial support of the Leverhulme Trust for this research project.

A Matrices for representations III–V

The forms of representations α equal to IV and V that we choose to use are given below with the upper sign for α as IV and the lower sign for α as V.

$$\boldsymbol{M}^{\alpha}(\mathsf{a}) = \pm\begin{pmatrix} 0 & 1 & 0 \\ -1 & 0 & 0 \\ 0 & 0 & -1 \end{pmatrix},\ \boldsymbol{M}^{\alpha}(\mathsf{a}^2) = \begin{pmatrix} -1 & 0 & 0 \\ 0 & -1 & 0 \\ 0 & 0 & 1 \end{pmatrix},\ \boldsymbol{M}^{\alpha}(\mathsf{a}^3) = \pm\begin{pmatrix} 0 & -1 & 0 \\ 1 & 0 & 0 \\ 0 & 0 & -1 \end{pmatrix},$$

$$\boldsymbol{M}^{\alpha}(\mathsf{b}) = \pm\begin{pmatrix} -1 & 0 & 0 \\ 0 & 0 & 1 \\ 0 & -1 & 0 \end{pmatrix},\ \boldsymbol{M}^{\alpha}(\mathsf{b}^2) = \begin{pmatrix} 1 & 0 & 0 \\ 0 & -1 & 0 \\ 0 & 0 & -1 \end{pmatrix},\ \boldsymbol{M}^{\alpha}(\mathsf{b}^3) = \pm\begin{pmatrix} -1 & 0 & 0 \\ 0 & 0 & -1 \\ 0 & 1 & 0 \end{pmatrix},$$

$$\boldsymbol{M}^{\alpha}(\mathsf{c}) = \pm\begin{pmatrix} 0 & 0 & -1 \\ 0 & -1 & 0 \\ 1 & 0 & 0 \end{pmatrix},\ \boldsymbol{M}^{\alpha}(\mathsf{c}^2) = \begin{pmatrix} -1 & 0 & 0 \\ 0 & 1 & 0 \\ 0 & 0 & -1 \end{pmatrix},\ \boldsymbol{M}^{\alpha}(\mathsf{c}^3) = \pm\begin{pmatrix} 0 & 0 & 1 \\ 0 & -1 & 0 \\ -1 & 0 & 0 \end{pmatrix},$$

$$\boldsymbol{M}^{\alpha}(\mathsf{d}) = \begin{pmatrix} 0 & 0 & 1 \\ 1 & 0 & 0 \\ 0 & 1 & 0 \end{pmatrix},\ \boldsymbol{M}^{\alpha}(\mathsf{d}^2) = \begin{pmatrix} 0 & 1 & 0 \\ 0 & 0 & 1 \\ 1 & 0 & 0 \end{pmatrix},\ \boldsymbol{M}^{\alpha}(\mathsf{e}) = \begin{pmatrix} 0 & 0 & -1 \\ -1 & 0 & 0 \\ 0 & 1 & 0 \end{pmatrix},$$

$$\boldsymbol{M}^{\alpha}(\mathsf{e}^2) = \begin{pmatrix} 0 & -1 & 0 \\ 0 & 0 & 1 \\ -1 & 0 & 0 \end{pmatrix},\ \boldsymbol{M}^{\alpha}(\mathsf{f}) = \begin{pmatrix} 0 & 0 & 1 \\ -1 & 0 & 0 \\ 0 & -1 & 0 \end{pmatrix},\ \boldsymbol{M}^{\alpha}(\mathsf{f}^2) = \begin{pmatrix} 0 & -1 & 0 \\ 0 & 0 & -1 \\ 1 & 0 & 0 \end{pmatrix},$$

$$\boldsymbol{M}^{\alpha}(\mathsf{g}) = \begin{pmatrix} 0 & 0 & -1 \\ 1 & 0 & 0 \\ 0 & -1 & 0 \end{pmatrix},\ \boldsymbol{M}^{\alpha}(\mathsf{g}^2) = \begin{pmatrix} 0 & 1 & 0 \\ 0 & 0 & -1 \\ -1 & 0 & 0 \end{pmatrix},\ \boldsymbol{M}^{\alpha}(\mathsf{h}) = \pm\begin{pmatrix} 1 & 0 & 0 \\ 0 & 0 & -1 \\ 0 & -1 & 0 \end{pmatrix},$$

$$\boldsymbol{M}^{\alpha}(\mathsf{j}) = \pm\begin{pmatrix} 0 & 0 & -1 \\ 0 & 1 & 0 \\ -1 & 0 & 0 \end{pmatrix},\ \boldsymbol{M}^{\alpha}(\mathsf{k}) = \pm\begin{pmatrix} 0 & -1 & 0 \\ -1 & 0 & 0 \\ 0 & 0 & 1 \end{pmatrix},\ \boldsymbol{M}^{\alpha}(\mathsf{l}) = \pm\begin{pmatrix} 1 & 0 & 0 \\ 0 & 0 & 1 \\ 0 & 1 & 0 \end{pmatrix},$$

$$\boldsymbol{M}^{\alpha}(\mathsf{m}) = \pm\begin{pmatrix} 0 & 0 & 1 \\ 0 & 1 & 0 \\ 1 & 0 & 0 \end{pmatrix},\ \boldsymbol{M}^{\alpha}(\mathsf{n}) = \pm\begin{pmatrix} 0 & 1 & 0 \\ 1 & 0 & 0 \\ 0 & 0 & 1 \end{pmatrix},\ \boldsymbol{M}^{\alpha}(\mathsf{i}) = \begin{pmatrix} 1 & 0 & 0 \\ 0 & 1 & 0 \\ 0 & 0 & 1 \end{pmatrix}.$$

The form of representation III that we use is given explicitly by

$$\boldsymbol{M}^{\mathrm{III}}(\mathsf{i}) = \boldsymbol{M}^{\mathrm{III}}(\mathsf{a}^2) = \boldsymbol{M}^{\mathrm{III}}(\mathsf{b}^2) = \boldsymbol{M}^{\mathrm{III}}(\mathsf{c}^2) = \begin{pmatrix} 1 & 0 \\ 0 & 1 \end{pmatrix},$$

$$\boldsymbol{M}^{\mathrm{III}}(\mathsf{a}) = \boldsymbol{M}^{\mathrm{III}}(\mathsf{a}^3) = \boldsymbol{M}^{\mathrm{III}}(\mathsf{k}) = \boldsymbol{M}^{\mathrm{III}}(\mathsf{n}) = \begin{pmatrix} -1 & 0 \\ 0 & 1 \end{pmatrix},$$

$$\boldsymbol{M}^{\mathrm{III}}(\mathsf{b}) = \boldsymbol{M}^{\mathrm{III}}(\mathsf{b}^3) = \boldsymbol{M}^{\mathrm{III}}(\mathsf{h}) = \boldsymbol{M}^{\mathrm{III}}(\mathsf{l}) = \frac{1}{2}\begin{pmatrix} 1 & -\sqrt{3} \\ -\sqrt{3} & -1 \end{pmatrix},$$

$$\boldsymbol{M}^{\mathrm{III}}(\mathsf{c}) = \boldsymbol{M}^{\mathrm{III}}(\mathsf{c}^3) = \boldsymbol{M}^{\mathrm{III}}(\mathsf{j}) = \boldsymbol{M}^{\mathrm{III}}(\mathsf{m}) = \frac{1}{2}\begin{pmatrix} 1 & \sqrt{3} \\ \sqrt{3} & -1 \end{pmatrix},$$

$$\boldsymbol{M}^{\mathrm{III}}(\mathsf{d}) = \boldsymbol{M}^{\mathrm{III}}(\mathsf{e}) = \boldsymbol{M}^{\mathrm{III}}(\mathsf{f}) = \boldsymbol{M}^{\mathrm{III}}(\mathsf{g}) = \frac{1}{2}\begin{pmatrix} -1 & \sqrt{3} \\ -\sqrt{3} & -1 \end{pmatrix},$$

$$\boldsymbol{M}^{\mathrm{III}}(\mathsf{d}^2) = \boldsymbol{M}^{\mathrm{III}}(\mathsf{e}^2) = \boldsymbol{M}^{\mathrm{III}}(\mathsf{f}^2) = \boldsymbol{M}^{\mathrm{III}}(\mathsf{g}^2) = \frac{1}{2}\begin{pmatrix} -1 & -\sqrt{3} \\ \sqrt{3} & -1 \end{pmatrix}.$$

B Degrees of freedom for representations I–V

We work with the modes in $\mathcal{G}_N$ given in (4.9) and here we let M be the number of degrees of freedom for a given value of N. In other words M is the minimum number of independent complex quantities needed to specify any field $\boldsymbol{b}$ in $\mathcal{G}_N$ for representations I and II, and to specify the fields $\boldsymbol{b}_j$ for representations III–V. In each case we include the constraint that $\nabla \cdot \boldsymbol{b} = 0$, but we do not impose Hermitian symmetry.

We consider a slice of constant l depicted in figure 5(a). We first note that in view of the discussion of section 4.2, the left-hand column $\boldsymbol{b}_{l,0,n}$, $0 < n < l$ and top row $\boldsymbol{b}_{l,m,l}$, $0 < m < l$ can be obtained from $\boldsymbol{b}_{l,n,0}$ and $\boldsymbol{b}_{l,l,m}$ respectively, using (4.6) and (4.7). The remaining modes are treated as follows for $\boldsymbol{b} \equiv \boldsymbol{b}_1$ in representations I and II, and the $\boldsymbol{b}_j$ for III–V.

- Modes $(\boldsymbol{b}_j)_{l,m,n}$, $(\boldsymbol{b}_j)_{l,m,0}$ and $(\boldsymbol{b}_j)_{l,l,n}$ with $0 < m, n < l$ are unconstrained and each corresponds to 2 degrees of freedom using (4.28).
- The modes $(\boldsymbol{b}_j)_{l,l,l}$ map to themselves under d and this constrains $\boldsymbol{b}_{l,l,l} = 0$ for representations I and II. For III, these modes are constrained to the form

$$(\boldsymbol{b}_1)_{l,l,l} = (2\alpha, -\alpha + \sqrt{3}\beta, -\alpha + \sqrt{3}\beta), \tag{B.1}$$
$$(\boldsymbol{b}_2)_{l,l,l} = (2\beta, -\sqrt{3}\alpha - \beta, \sqrt{3}\alpha - \beta). \tag{B.2}$$

  For IV and V the fields must take the form

$$(\boldsymbol{b}_1)_{l,l,l} = (\alpha, -\alpha - \beta, \beta), \quad (\boldsymbol{b}_2)_{l,l,l} = (\beta, \alpha, -\alpha - \beta), \quad (\boldsymbol{b}_3)_{l,l,l} = (-\alpha - \beta, \beta, \alpha). \tag{B.3}$$

- The modes $(\boldsymbol{b}_j)_{l,l,0}$ map to themselves under k and this constrains $\boldsymbol{b}_{l,l,0} = 0$ for I and

$$\boldsymbol{b}_{l,l,0} = (\alpha, -\alpha, \beta) \tag{B.4}$$

for II. For representation III, however, the two fields take the form

$$(\boldsymbol{b}_1)_{l,l,0} = (\alpha, -\alpha, \beta), \quad (\boldsymbol{b}_2)_{l,l,0} = 0 \tag{B.5}$$

For IV the fields must take the form

$$(\boldsymbol{b}_1)_{l,l,0} = (\boldsymbol{b}_2)_{l,l,0} = (\alpha, -\alpha, \beta), \quad (\boldsymbol{b}_3)_{l,l,0} = 0. \tag{B.6}$$

and for V

$$(\boldsymbol{b}_1)_{l,l,0} = (\alpha, -\alpha, \gamma), \quad (\boldsymbol{b}_2)_{l,l,0} = (-\alpha, \alpha, -\gamma), \quad (\boldsymbol{b}_3)_{l,l,0} = (\beta, -\beta, \delta). \tag{B.7}$$

- The modes $(\boldsymbol{b}_j)_{l,0,0}$ map to themselves under b. For representations I (upper sign) and II (lower sign) this constrains $\boldsymbol{b}_{l,0,0} = 0$ for $l = 2k$ even, and

$$\boldsymbol{b}_{l,0,0} = (0, \alpha, \mp(-1)^k i\alpha), \tag{B.8}$$

for $l = 2k - 1$ odd. For representation III, the fields are of the form

$$(\boldsymbol{b}_1)_{l,0,0} = 0, \quad (\boldsymbol{b}_2)_{l,0,0} = 0 \tag{B.9}$$

for $l = 2k$ even and

$$(\boldsymbol{b}_1)_{l,0,0} = (0, 2\alpha, (-1)^k i(\sqrt{3}\beta - \alpha)), \quad (\boldsymbol{b}_2)_{l,0,0} = (0, 2\beta, (-1)^k i(\sqrt{3}\alpha + \beta)) \tag{B.10}$$

for $l = 2k - 1$ odd. For IV (upper sign) and V (lower sign) the fields must take the form

$$(\boldsymbol{b}_1)_{l,0,0} = 0, \quad (\boldsymbol{b}_2)_{l,0,0} = (0, \alpha, \pm(-1)^k \beta), \quad (\boldsymbol{b}_3)_{l,0,0} = (0, \beta, \mp(-1)^k \alpha) \tag{B.11}$$

for $l = 2k$ even, and

$$(\boldsymbol{b}_1)_{l,0,0} = (0, \alpha, \pm(-1)^k i\alpha), \quad (\boldsymbol{b}_2)_{l,0,0} = 0, \quad (\boldsymbol{b}_3)_{l,0,0} = 0 \tag{B.12}$$

for $l = 2k - 1$ odd.

Counting of modes gives the the total number of degrees of freedom as

$$M = \tfrac{1}{6}(4N^3 - 6N^2 - 7N + 12), \tag{B.13}$$
$$M = \tfrac{1}{6}(4N^3 - 6N^2 + 5N), \tag{B.14}$$
$$M = \tfrac{1}{3}(4N^3 - 6N^2 + 5N), \tag{B.15}$$
$$M = \tfrac{1}{2}(4N^3 - 6N^2 + N), \tag{B.16}$$
$$M = \tfrac{1}{2}(4N^3 - 6N^2 + 5N - 4), \tag{B.17}$$

for I, II, III, IV, V respectively for N even, while for N odd,

$$M = \tfrac{1}{6}(4N^3 - 6N^2 - 7N + 9), \tag{B.18}$$
$$M = \tfrac{1}{6}(4N^3 - 6N^2 + 5N - 3), \tag{B.19}$$
$$M = \tfrac{1}{3}(4N^3 - 6N^2 + 5N - 3), \tag{B.20}$$
$$M = \tfrac{1}{2}(4N^3 - 6N^2 + N + 1), \tag{B.21}$$
$$M = \tfrac{1}{2}(4N^3 - 6N^2 + 5N - 3). \tag{B.22}$$

References

Alexakis, A. 2011 Searching for the fastest dynamo: laminar ABC flows. *Phys. Rev. E* **84**, 026321.

Archontis, V. & Dorch, B. 1999 Numerical simulations of dynamos associated with ABC flows. In: *Workshop on stellar dynamos, ASP conference series* (ed. Nunez, M. & Ferriz-Mas, A.), vol. 178, pp. 1–11.

Archontis, V., Dorch, S.B.F & Nordlund, A.A. 2003 Numerical simulations of kinematic dynamo action. *Astron. & Astrophys.* **397**, 393–399.

Arnold, V.I. 1965 Sur la topologie des écoulements stationnaires des fluides parfaits. *C.R. Acad. Sci. Paris* **261**, 17–20.

Arnold, V.I. 1984 On the evolution of a magnetic field under the action of transport and diffusion. In *Some questions in modern analysis* (ed. V.M. Tikhomirov), *Mekh.-Mat. Fak. Moskov. Gos. Univ.*, pp. 8–21. Translated in *Fourteen papers translated from the Russian*, *Am. Math. Soc. Transl.*, series 2, vol. 137, pp. 119–129 (1987).

Arnold, V.I. & Korkina, E.I. 1983 The growth of a magnetic field in a three-dimensional steady incompressible flow. *Vest. Mosk. Un. Ta. Ser. 1, Matehm. Mekh.*, no. 3, 43–46.

Ashwin, P. & Podvigina, O. 2003 Hopf bifurcation with cubic symmetry and instability of ABC flow. *Proc. R. Soc. Lond. A* **459**, 1801–1827.

Bouya, I. & Dormy, E. 2013 Revisiting the ABC flow dynamo. *Phys. Fluids*, in press.

Childress, S. 1970 New solutions of the kinematic dynamo problem. *J. Math. Phys.* **11**, 3063–3076.

Childress, S. & Gilbert, A.D. 1995 *Stretch, twist, fold: the fast dynamo*. Springer-Verlag.

Clyne, J., Mininni, P., Norton, A. & Rast, M. Interactive desktop analysis of high resolution simulations: application to turbulent plume dynamics and current sheet formation. *New J. Phys.* **9**, 301–329.

Dombre, T. Frisch, U., Greene, J.M., Hénon, M., Mehr, A. & Soward, A.M. 1986 Chaotic streamlines in the ABC flows. *J. Fluid Mech.* **167**, 353–391.

Dorch, S. B. F. 2000 On the structure of the magnetic field in a kinematic ABC flow dynamo. *Physica Scripta* **61**, 717–722

Finn, J.M., Hanson, J.D., Kan, I. & Ott, E. 1991 Steady fast dynamo flows. *Phys. Fluids B* **3**, 1250–1269.

Galanti, B., Pouquet, A. and Sulem, P.-L. 1992 Linear and nonlinear dynamos associated with ABC flows. *Geophys. Astrophys. Fluid Dynam.* **66**, 183–208.

Galloway, D. 2012 ABC flows then and now. *Geophys. Astrophys. Fluid Dynam.* **106**, 450–467.

Galloway, D. & Frisch, U. 1986 Dynamo action in a family of flows with chaotic streamlines. *Geophys. Astrophys. Fluid Dynam.* **36**, 53–83.

Galloway, D.J. & Frisch, U. 1987 A note on the stability of a family of space-period Beltrami flows. *J. Fluid Mech.* **180**, 557–564.

Galloway, D.J. & O'Brian, N.R. 1994 Numerical calculations of dynamos for ABC and related flows In: *Solar and planetary dynamos* (Ed. Proctor, M.R.E., Matthews, P.C. & Rucklidge, A.M.), Cambridge University Press.

Gilbert, A.D. 1988 Fast dynamo action in the Ponomarenko dynamo. *Geophys. Astrophys. Fluid Dynam.* **44** 214–258.

Gilbert, A.D. 1992 Magnetic field evolution in steady chaotic flows. *Phil. Trans. R. Soc. Lond. A* **339**, 627–656.

Gilbert, A.D., Ponty, Y. & Zheligovsky, V. 2011 Dissipative structures in a nonlinear dynamo. *Geophys. Astrophys. Fluid Dynam.* **105**, 629–653.

Hamermesh, M. 1962 *Group theory and its application to physical problems.* Addison-Wesley

Hénon, M. 1966 Sur la topologie des lignes de courant dans un cas particulier. *C.R. Acad. Sci. Paris A* **262**, 312–314.

Klapper, I. & Young, L.-S. 1995 Rigorous bounds on the fast dynamo growth rate involving topological entropy. *Comm. Math. Phys.* **173**, 623–646.

Lau, Y.-T. & Finn, J.M. 1993 Fast dynamos with finite resistivity in steady flows with stagnation points. *Phys. Fluids B* **5**, 365–375.

Matthews, P.C. 1999 Dynamo action in simple convective flows. *Proc. R. Soc. Lond. A* **455**, 1829–1840.

Moffatt, H.K. & Proctor, M.R.E. 1985 Topological constraints associated with fast dynamo action. *J. Fluid Mech.* **154**, 493–507.

Podvigina, O. & Pouquet, A. 1994 On the nonlinear stability of the 1:1:1 ABC flow. *Physica D* **75**, 471–508.

Podvigina, O. 1999 Spatially-periodic steady solutions to the three-dimensional Navier–Stokes equation with the ABC force. *Physica D* **128**, 250–272.

Ponomarenko, Yu.B. 1973 On the theory of hydromagnetic dynamos. *Zh. Prikl. Mekh. & Tekh. Fiz.* **6**, 47–51.

Ruzmaikin, A.A., Sokoloff, D.D. & Shukurov, A.M. 1988 A hydromagnetic screw dynamo. *J. Fluid Mech.* **197**, 39–56.

Trefethen, L.N. & Bau, D. 1997 *Numerical linear algebra.* SIAM, Philadelphia.